scientific reports

Check for updates

OPEN

Influence of post-fire recuring regimes on the properties of self-compacting concrete with heavyweight aggregate

Taher A. Tawfik[1,2]✉, Martin T. Palou[1], František Šoukal[3], Eva Kuzielová[4], Peter Peciar[5], Mahmoud Gharieb[6], Sheelan Mahmoud Hama[7] & Jozef Švorec[4]

Fire safety is essential in construction, as accidental fires subject concrete structures to high temperatures that result in significant damage. This study examines the development of self-compacting concrete (SCC) characteristics with barite heavyweight aggregate (20–100% substitution of natural coarse aggregate) after being exposed to 600 °C, followed by several post-fire re-curing methods (water, CO_2, water-glass, and air). The property evolution was examined for cracking, density loss, residual compressive strength, and ultrasonic behavior, verified by FTIR, MIP, and SEM–EDX tests. The exposure to 600 °C resulted in widespread microcracking, significant mass loss, and decreased strength, besides the severity increasing with higher barite concentrations due to the brittleness and thermal sensitivity of heavyweight aggregate. Post-fire curing demonstrated specific recovery mechanisms: water curing promoted rehydration and achieved partial strength recovery of approximately 75% of pre-fire values; CO_2 curing improved densification via carbonation but resulted in increased brittleness; water-glass curing partially filled cracks but decreased long-term stability; and air curing caused additional drying shrinkage and further deterioration. The results highlight the interrelated chemical and microstructural changes that influence the post-fire development of SCC characteristics, revealing that water and CO_2 re-curing are the most effective methods for performance restoration.

Keywords Self-compacting concrete (SCC), Heavyweight concrete (HWC), 600 °C, Post-fire-curing, Recovery, Residual performance, Microstructure

A primary factor that must be considered in the designing and planning of structural buildings is fire safety because of the exposure to elevated temperatures in an accident event or while in the operation process[1]. While the rise in temperature during operation is predicable, the occurrence of an accidental fire is unforeseeable, which may lead to mortality and significant asset damage. According to the aforementioned factors, the concrete was regularly used because it was characterized by its resistance to fire[2]. The definition of fire resistance could be stated as the ability of various components of a structure to tolerate the exposure to fire and act according to their function of load-bearing[3]. The concrete is essentially formed from a combination of coarse and fine aggregates, which are held together by a paste of cement[4]. The concrete withstands the increase in temperature until a certain threshold, which was according to previous studies at 200 °C, as the alteration in microstructure and loss of strength were minimal[5–7]. As the temperature increases, concrete begins to suffer from several damages. These damages include a decrease in strength, a loss of weight, pore expansion, attenuation of elastic modulus, spalling, crack propagation[8], as well as damage to the microstructure, which was clearly visible after 300 °C[7,9–12]. The deterioration of concrete at extreme temperatures may be attributed to three primary factors: the breakdown of

[1]Institute of Construction and Architecture, Slovak Academy of Sciences, Dúbravská cesta 9, Bratislava SK-845 03, Slovak Republic. [2]Department of Construction and Building Engineering, High Institute of Engineering, October 6 City, Egypt. [3]Institute of Materials Science, Faculty of Chemistry, Brno University of Technology, Brno 612 00, Czech Republic. [4]Faculty of Chemical and Food Technology, Slovak University of Technology, Radlinského 9, Bratislava SK-812 37, Slovak Republic. [5]Faculty of Mechanical Engineering, Slovak University of Technology, Námestie slobody 17, Bratislava SK-812 31, Slovak Republic. [6]Raw Building Materials Technology and Processing Research Institute, Housing & Building National Research Center, HBRC, Cairo, Egypt. [7]Civil Engineering Department, University of Anbar, Ramadi, Iraq. ✉email: taher@savba.sk

hydration products, the formation of internal vapor pressure, and the ingredients' thermal incompatibility[13,14]. The decomposition of the cement matrix occurred during the exposure to elevated temperature, leading to an alteration within the microstructure, triggering the development of thermal cracks, and ultimately resulting in substrate spalling[15,16].

The area that is highly prone to heat cracking is known as the interfacial transition zone (ITZ), characterized as the most fragile connection among components of concrete[17]. When exposed to elevated temperatures, aggregates tend to expand, while a shrinkage may be observed in the binder. This discrepancy has a negative impact on the interfacial transition zone and worsens the concrete mechanical properties[18,19]. The rise in the cement paste volume causes a further increase in the risk, as well as a rapid increase in the strength of concrete[10]. It is essential to assess the characteristics of self-compacting concrete (SCC) when exposed to an elevated temperature, considering that SCC often has a significant amount of binder-paste[6]. In addition, high-performance concrete, such as self-compacting concrete, is usually characterized by minimal permeability and porosity. This hinders the release of trapped accumulative moisture, which is released from the decomposition of hydrates, and can result in higher internal vapour pressure, as well as deteriorating the residual characteristics of SCC even more in elevated temperature exposures compared to conventional concrete[15].

Lately, Heavyweight concrete (HWC) has gained significant attention in recent years as a highly cost-effective concrete technology alongside SCC. It is not only utilized to construct sustainable structures characterized by extended lifespans, but also to minimize effects on the environment belonging to the construction sector[20]. Moreover, there has been a significant focus on integrating such technologies in order to expand their applications by developing distinct mechanical features that enhance performance in terms of structure. The manufacture of HWC was carried out through the replacement of NWA (normal weight aggregate) by heavyweight aggregate such as hematite, barite, iron, magnetite, etc. This innovative type of concrete exhibits exceptional properties for radiation protection. Concrete must possess a specific gravity of over 2600 kg/m^3 to be classified as HWC, whereas the density of HWA (heavyweight aggregate) reaches a threshold of around 3000 kg/m^3[21]. In nuclear power facilities, HWC is the most suitable structural material due to its exceptional electromagnetic shielding efficiency, as protection from radioactive radiation is crucial[22]. Furthermore, several research investigations have illustrated that heavyweight concrete exhibits significantly greater fire resistance compared to ordinary concrete due to the increased HWA's thermal stability in comparison to normal weight aggregates (NWA)[22–26]. However, according to various studies, incorporating HWA into cement paste may adversely influence the fresh and mechanical properties of concrete. This is due to the presence of HWA (heavyweight aggregates), which is characterized by its high crystalline microstructure and great ability to absorb water[27,28].

In general, the concrete buildings damaged by fire could continue to serve after repairs. The most conventional repair methodology is to replace the layers which is destroyed by fresh concrete. The latest studies have revealed the usage of FRP (fiber-reinforced plastic) composites for mending fire-damaged concrete buildings[29,30]. The main drawback is that both repair approaches necessitate more resource consumption, such as materials needed to produce fresh concrete or FRP composites, as well as significant labor for the repair process. Numerous investigations have illustrated that the properties of concrete damaged by fire, such as total porosity and pore size, strength, and cracks, could possibly be restored through adequate curing in a suitable environment following exposure[31–35].

According to previous studies, the concrete recovery that is damaged by fire could be related to the rehydration of the dehydrated products that were formed at elevated temperatures[32,33,36,37]. X-ray diffraction (XRD) and[29] Si magic angle spinning nuclear magnetic resonance (MAS-NMR) were employed by Alonso et al.[38] to examine the rehydration and dehydration procedures of cement paste exposed to high temperatures of 100, 200, 450, and 750 °C for 2 h. Based on their NMR observations, the maximum transformation occurred at 450 °C, where C-S-H chains were formed solely by silicate dimers. After 750 °C, a complete disappearance of the C-S-H gel was observed. Ettringite had already disappeared below 100 °C, and calcite was almost completely decomposed after firing at 750 °C. However, these dehydrated substances can regain their water content when subjected to a re-curing process in a sufficiently wet environment. Shui et al. reported a similar observation[39], which demonstrated that pastes prepared from powdered samples dehydrated at 400, 600, and 800 °C, and subjected to a fog-spraying curing regime, almost reached 70% rehydration after just 1 day, irrespective of the dehydration temperature. Furthermore, they observed that the rehydrated structure becomes denser as the temperature increases. Li et al.[40] reviewed various curing procedures after fire exposure, the recovery techniques, and the effect of recovery regimes on mechanical characteristics, durability, pore structure, cracks, and chemical properties. They confirmed that the rehydration of dehydrated products in fire-damaged concrete is a water-ingress-controlled process; however, the speed of rehydration does not directly determine the rate of compressive strength recovery. Qian et al.[41] identified constraints in post-fire strength recovery, achieving just 15–20% restoration using water re-curing. Various techniques can be employed to provide water to fire-damaged concrete in order to facilitate rehydration. The post-fire-curing procedures might be categorized into three types based on the techniques for providing water. Firstly, for air post-fire-curing, after being exposed to high temperatures, samples were immediately cured in the air[35,42]. Secondly, for water–air post-fire-curing, the samples were immersed in water for a certain duration and subsequently cured in the air under controlled relative humidity[43,44]. Thirdly, for water post-fire curing, the samples were completely immersed in water throughout the post-fire curing procedure[32,43]. The latest studies on SCC fire resistance have highlighted the effectiveness of post-fire re-curing techniques. A study conducted by Onyelowe et al.[45], illustrated that water re-curing of hybrid fiber SCC after being exposed to high-temperature fosters huge mechanical recovery. Additionally, Bouhafs et al.[46] observed that recurred water significantly improved microstructural densification and restored strength through SEM/MIP analysis. The restoration of the remaining ultrasonic pulse velocity and the compressive strength of fire-damaged concrete that was immersed in water for varying periods was studied by Lin et al.[47]. The compressive strength of concrete exposed to temperatures of 600 °C, 500 °C, and 400 °C was restored by approximately 62%, 89%, and 78%,

respectively, within the initial 7 days. After 30 days, the compressive strength had recovered to about 65%, 98%, and 90%, respectively. However, concrete samples exposed to temperatures exceeding 800 °C did not experience significant recovery in compressive strength through post-fire curing. Furthermore, it was observed that the samples' relative residual compressive strength increased from 77 to 83% after post-fire-curing when chilled by the air and from 65 to 87% when chilled in the furnace[48].

As indicated by the findings of the literature review, many researchers have investigated the effect of post-fire curing on the characteristics of conventional concrete. To the best of our knowledge, no study has yet focused on the impact of various post-fire curing regimes on the properties of SCC containing heavyweight aggregate as a partial substitution for normal weight aggregates for producing heavyweight SCC (HWSCC) after exposure to temperature. Thus, this study attempted to assess the effect of various post-fire curing regimes (re-curing using water, CO_2, water glass, and air) on the density loss, residual compressive strength, ultrasonic behaviour, and apparent property of SCC following exposure to 600 °C. SCC incorporated various proportions of coarse aggregate of barite heavyweight with a particle size ranging from 4 to 8 mm at 100%, 80%, 60%, 40%, and 20%, replacing natural coarse aggregate Structural changes in the binder resulting from firing, as well as various post-firing treatment regimes, were assessed by Fourier Transform Infrared Radiation (FTIR). Mercury Intrusion Porosimetry (MIP), along with Scanning Electron Microscopy (SEM) and Energy Dispersive X-ray Spectroscopy (EDX), was used to investigate the microstructure development of heated and re-cured SCC samples.

Experimental program

Materials

In the current research, GGBFS (Ground Granulated Blast Furnace Slag), Portland cement, Sand, silica fume (SF), Barite, Superplasticizers, and Gravel were utilized. The concrete mixtures were developed using CEM I 42.5 R cement, which possessed a specific gravity and a fineness of values 3.15 and 3800 cm^2/g, respectively. The specific gravity of SF and GGBFS was 2.15 and 2.95, respectively, with corresponding fineness values of 15×104 cm^2/g and 4.17 cm^2/g, respectively. Table 1 illustrates chemical analysis of the employed barite, GGBFS, SF, and cement. NWA was made out of coarse gravel aggregates graded constantly, with sizes ranging from 4 to 8 mm and 8–16 mm, and river sand measuring 0/4 mm. While HWA was made out of barite, measuring the size of 4–8. The barite and sand with a particle size of 4–8 mm, as well as the gravel with particle sizes of 4–8 mm and 8–16 mm, exhibited 1.47%, 1.2%, 1%, and 1% water absorption capacities, respectively. The barite and sand with a particle size of 4–8 mm, as well as the gravel with particle sizes of 4–8 mm and 8–16 mm, possessed specific gravities of 4.2, 2.65, 2.67, and 2.67, respectively. Moreover, the barite strength was assessed by conducting impact values and aggregate crushing experiments, yielding values of 41.5% and 43% for these variables, respectively. The flakiness and elongation index of barite are 36% and 14%, respectively, and water absorption is 0.7%. In order to improve the workability of concrete and decrease its viscosity, the HWSCC implemented STACHEMENT 2014, a polycarboxylic ether-based superplasticizer produced by STACHEMA Bratislava Chemical Company in Slovakia.

Manufacturing of concrete

Substituting 100%, 80%, 60%, 40%, 20%, and 0% of natural coarse aggregates, which have a size range of 4–8, with barite aggregates of the same size range (4–8), in 6 mix designs, known as SCC-100, SCC-80, SCC-60, SCC-40, SCC-20, and SCC-0, were conducted, respectively. HWSCC-0 was employed as a reference mix without any HWA. The fresh test for concrete was carried out following the code of EFNARC (2002, 2005). In order to achieve a comparable performance, the cementitious materials quantity (SF + GGBFS + cement) used (462.82 kg/m^3) was maintained at a consistent level. Additionally, a concentration of 1.2% relative to the weight of the cementitious

Chemical constituent	Barite aggregate (%)	GGBFS (%)	Silica fume (%)	Cement (%)
Al_2O_3	1.2	8.50	0.21	4.43
Fe_2O_3	2.1	0.24	-	2.60
SiO_2	0.1	37.20	97.10	19.10
CaO	0.04	38.90	0.5	63.80
TiO_2	0.02	0.30	-	0.25
MnO	-	0.51	-	0.19
K_2O	-	0.36	-	0.53
MgO	0.06	10.20	0.4	2.39
Na_2O	0.31	0.46	-	0.41
P_2O_5		0.02	-	0.09
Cl^{-1}	0.08	0.03	-	0.09
SO_3	28.2	3.01	-	3.49
SrO	-	0.06	-	0.02
BaO	65.9	0.08	-	0.03
P2O5	0.06	-	-	-
Loss by Annealing	1.2	0.36	-	2.31

Table 1. Chemical analysis of barite, slag, cement, and silica fume used (mass %).

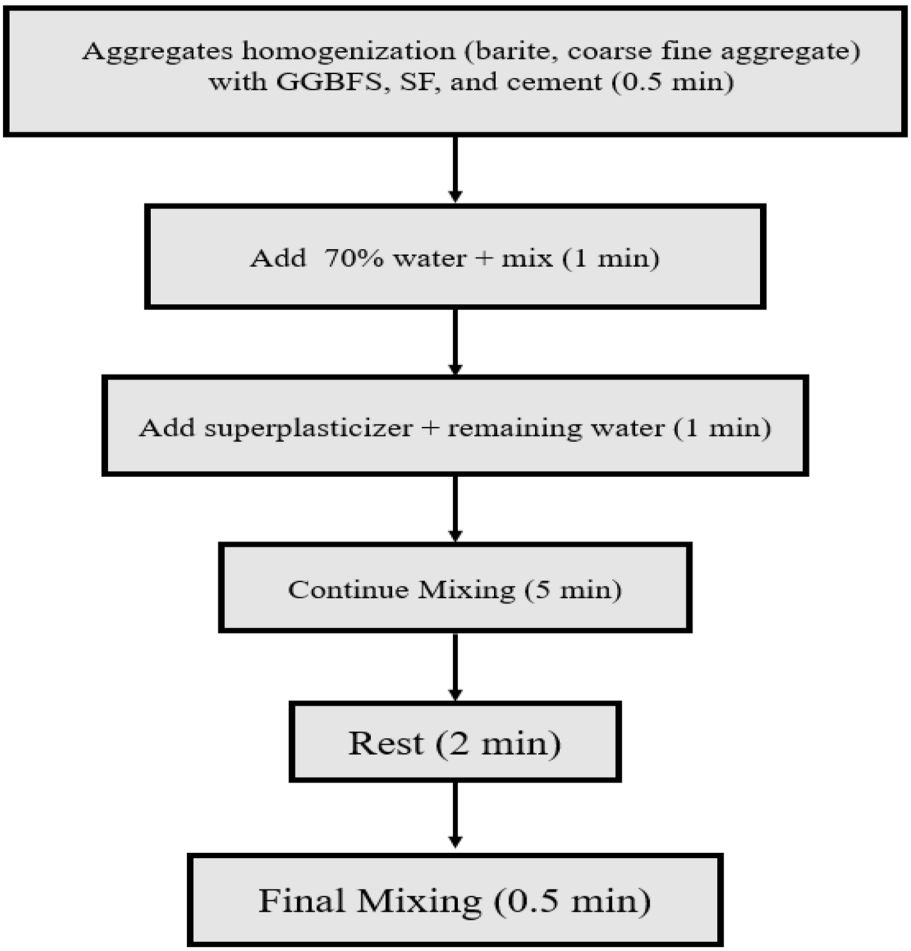

Fig. 1. Mixing process of SCC mixtures.

MIX ID	SP	Water	FA	NC (8–16)	HW aggregate (4–8)	NC aggregate (4–8)	SF	GGBFS	Cement
SCC-0	5.56	185	867	560	0	280	28.11	85.85	348.86
SCC-20	5.56	185	867	560	88.090	224	28.11	85.85	348.86
SCC-40	5.56	185	867	560	176.180	168	28.11	85.85	348.86
SCC-60	5.56	185	867	560	264.270	112	28.11	85.85	348.86
SCC-80	5.56	185	867	560	352.360	56	28.11	85.85	348.86
SCC-100	5.56	185	867	560	440.449	0	28.11	85.85	348.86

Table 2. Current experimental program mix proportions in the research (kg/m^3). SCC-0: self-compacting concrete control mixture excluding the usage of waste barite of size ranging from 4 to 8 mm. HWSCC-20: 20% barite size (4–8) of Self-compacting concrete by volume of coarse aggregate size (4–8).

materials was also used to dose the HRWR. The methodology and schedule for the execution of mixed designs were shown in (Fig. 1). The specification of the concrete's mixture design is shown in Table 2. Following the casting process, the samples were placed under a plastic sheet. After 24 h, specimens were removed from the molds and cured in water at a temperature of 25 ± 2 °C. This curing process continued until the specimens were subjected to a temperature of 600 °C after 28 days.

The procedures of tests

The test of fresh concrete

Several workability tests were executed on SSC mixes such as T500, slump-flow, J-ring, V-funnel, and L-Box, in accordance with the EFNARC specification[49,50], where the process for conducting each examination is illustrated in (Fig. 2). The ability of self-compacting concrete (SCC) to flow through reinforcing bars and its resistance to obstruction were evaluated by L-box and J-ring tests. The flow time T500 is the duration required to achieve a 500 mm flow diameter. The viscosity of the SCC was measured using the T500 method and the V-funnel test. The

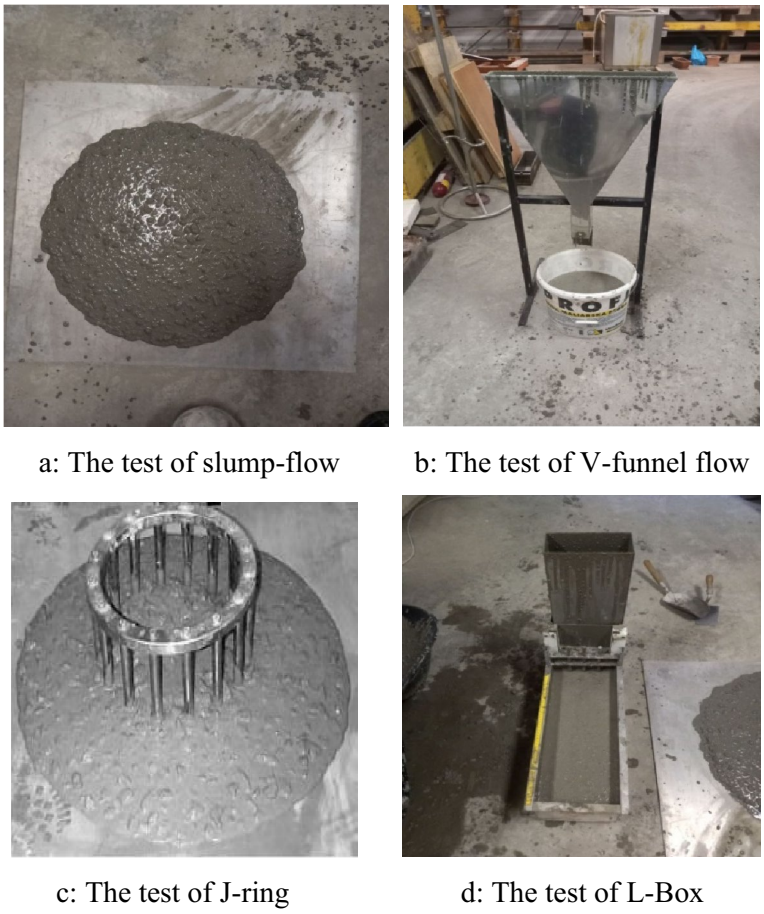

Fig. 2. Fresh concrete tests.

test of the V-funnel was performed to ascertain the duration of flow required for the mix to leave the funnel. The slump flow test was executed to inspect the bleeding, flowability, and segregation of the SSC mix. The slump-flow diameter was identified by calculating the average of the two immense SSC diameters.

The test of hardened concrete

Compressive strength Thereafter, the samples were cured in water for 7 and 28 days, and compressive strength testing was performed according to the EN 2390-3[51]. As illustrated in Fig. 3a, the 100 mm cubes were compressed at a consistent loading rate of 0.4 MPa/s until the samples failed, using compression testing equipment having a capacity of 2000 kN. The compressive strength1 of each mix was calculated by averaging the results of three cube specimens.

Dry density An investigation was conducted to determine the dry density of 100 mm cubes, using the guidelines of ASTM C 642, 2006[52], as illustrated in Fig. 3b The outcomes of the SCC examinations, which involved different ratios of barite dry density, were reported as the mean value of three samples.

Ultrasonic pulse velocity An investigation was performed to determine the ultrasonic pulse velocity of 100 mm cubes, using the guidelines of ASTM C 597, 2002[53]. The ultrasonic pulse velocity tests were conducted on 100 mm cubes following the guidelines of ASTM C 597-02[54]. The pulse velocity calculation was carried out by dividing the time of the pulse by the length of the path, as shown in the equation below. The findings of three samples were employed to calculate the mean ultrasonic pulse velocity of self-compacting concrete. The ultrasound setup test is shown in Fig. 3c.

$$V = {}^{L}/_{t}$$

where:

L = path length (km),
t = the duration of time (seconds),
V = velocity (km/sec).

Fig. 3. (**a**) Compressive strength, (**b**) dry density, and (**c**) ultrasonic pulse velocity test setup.

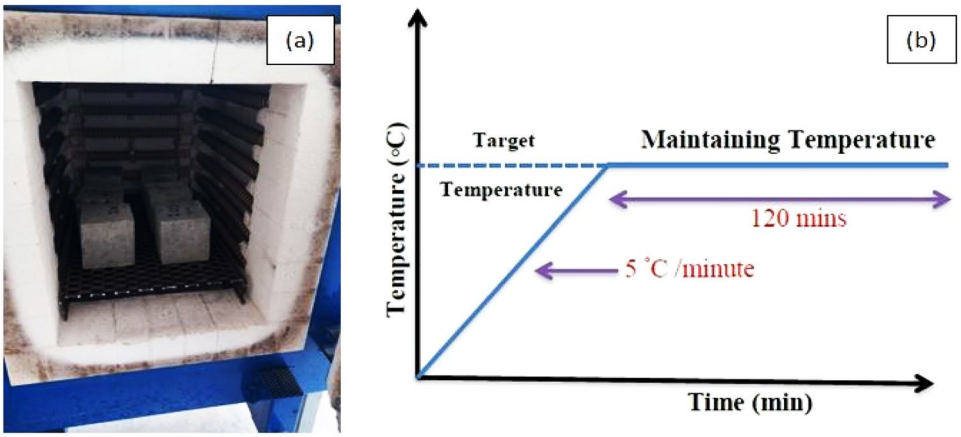

Fig. 4. (**a**) Electric furnace for high temperature; (**b**) Heating process.

Heating of concrete specimens

After 28 days, a control group of specimens that were not subjected to heat was evaluated to determine their compressive strength and dry density values. The remaining samples in the electric furnace (Fig. 4a) were exposed to a 600 °C temperature, where the temperature rose by 5 °C every minute. Once the desired maximum temperature was achieved, it was maintained at a constant level for two hours, as shown in Fig. 4b. After completing the process of heating, the specimens were permitted to cool gradually in air for 24 h after opening the oven door.

Post-fire recovery treatments

The thermally treated samples were classified into four categories in order to examine various post-fire-curing conditions: water-cured, air-cured, water glass-cured, and CO_2-cured samples. During the water-curing process, the samples of hot cubes were submerged in tap water, which simulated the actual fire application. However, during the air-curing process, the samples were air-cured at a temperature of 25 ± 2 °C and a relative humidity of 50% in a laboratory environment. Sodium water glass 2.0 (WG), produced by Vodní sklo a.s., in the Czech Republic, was used for water glass curing with characteristics specified in Table 3. The chamber for CO_2-curing maintained a CO_2 content of 20%, a temperature of 25 ± 1 °C, and a consistent relative humidity of 60 ± 5%, as determined by earlier research[55,56]. Figure 5 illustrates the 28-day curing period for each post-fire curing protocol.

After being subjected to several distinct treatment regimes, visual inspection was carried out on the samples in order to detect any signs of voids and cracks, and their remaining strength was assessed.

Examination of microstructure and formed phases

Scanning electron microscopy (SEM) with EDX analysis and mercury intrusion porosimetry (MIP) were conducted to investigate the microstructural characteristics of the concrete. The character of phases developed under different treatment regimes was studied using FTIR (Fourier Transform Infrared Spectroscopy).

To prevent the decomposition of hydrates, the samples for MIP and FTIR analyses were dried using a solvent-exchange method with diethyl ether and acetone. Pressure filtration was used to remove solvents, followed by vacuum drying. Pieces from the central parts of the samples were used.

SEM and EDX analyses were performed using a scanning electron microscope, Carl Zeiss EVO-LS10, Germany, and an Oxford X-Max 80 mm^2 (Oxford Instruments, UK) energy dispersive X-ray detector. Secondary electron imaging (SEI) mode was used to observe the morphology of the fracture surfaces, while backscattered electron (BSE) mode was applied to detect the presence of different phases in cross-sectional areas. An acceleration voltage of 15 kV was used, and EDX results were processed using the Oxford Aztec System. Au was used to sputter-coat samples before being observed.

A POREMASTER-60 GT device from Quantachrome Instruments UK Limited was used to perform mercury intrusion porosimetry. Multiple fragments, each with a diameter of less than 10 mm and a total mass not exceeding 1.5 g, were taken from various central regions of each dried sample. The maximum applied mercury pressure reached 420 MPa, corresponding to a minimum pore radius of 3.5 nm.

Thermo Scientific™ Nicolet-5700 FTIR was used to record the infrared spectra at room temperature. The records mid-IR (MIR) with a scanning range 4000~400 cm^{-1} were acquired with a DTGS detector, KBr beam splitter, and IR source. The KBr pellet method was utilized to collect the MIR transmission spectra, which involved homogenizing 200 mg of KBr with 1 mg of the specimen. For a period of 16 h at 50 °C, the KBr pellets were dried. A record for 64 scans was carried out, characterized by 4 cm^{-1} resolution for each specimen. The spectra processing was determined through the use of the "Thermo Scientific OMNIC Software Suite". Besides, the software was used in the detection of vibrational bands with accurate position through the Savitsky-Golay filter (second derivative function) that appeared due to inflections/ shoulders in the IR spectra.

Results and discussions

Fresh characteristics

All SCC mixtures were examined for workability according to EFNARC guidelines (slump-flow, J-ring, V-funnel, and L-box tests). The results of the study showed that mixtures containing up to 80% barite met SCC specifications, providing reliable casting and consistency in future residual property tests. Results are excluded here as this study concentrates on post-fire performance.

Fresh density of concrete

For the studied mixtures, the fresh concrete densities are illustrated in Fig. 6. The density of fresh concrete increased significantly through the incorporation of barite, characterized by aggregate size (4–8). Adding 100%, 80%, 60%, 40%, and 20% of barite led to an increase in density of 10.24%, 9.24%, 7.66%, 5.16%, and 1.21%, respectively, which is attributed to the barite specific gravity that is greater than natural coarse aggregate (4–8). Typically, the findings of the test concerning fresh concrete demonstrate that as the amount of barite increases, workability declines. The barite particles, characterized by higher density in comparison with natural coarse aggregate, cause a drop in workability (4–8). The concrete mixtures that contained barite coarse aggregate (4–8) up to 80% satisfied all of the SCC EFNARC recommended standards without any blockage or segregation. However, the 100% barite concrete did not meet most of the self-compacting concrete requirements, besides

Parameter	Value
Dry mass ($Na_2O + SiO_2$)/mass%	48.87
SiO_2 / Na_2O molar ratio	1.96
Density (20 °C)/kg m^{-3}	1.615
SiO_2 content/mass%	32.03
Na_2O content/mass%	16.84
pH	12.1

Table 3. Properties of the utilized sodium water glass given by the producer.

Fig. 5. Different curing methods after exposure to 600 °C: (**a**) Air-; (**b**) CO_2-; (**c**) water-; and (**d**) water glass-curing.

showing slight segregation. Therefore, concretes with up to 80% barite content meet the desired fresh properties of self-compacting concrete. However, those with 100% barite may be unsuitable for SCC.

Hardened characteristics

Dry density at ambient temperature

Figure 7 demonstrates the effects of employing various proportions of barite on the dry density of self-compacting concrete. The dry density of self-compacting concrete containing barite (4–8 mm) varies from 2468 kg/m^3 to 2650 kg/m^3. When the barite content within the mixes increases rather than the coarse aggregate size (4–8 mm), the dry density rises. A comparable pattern is observed in the hardened concrete density, as it is with the fresh concrete density. An increase in dry densities of 7.67%, 6.9%, 5.71%, 3.44%, and 1.13% was demonstrated for SCC-100, SCC-80, SCC-60, SCC-40, and SCC-20, respectively, compared to the reference mixture. Typically, concrete is categorized as HWC when its density exceeds 2600 kg/m^3[21]. Thus, the SCC specimens that had barite contents of 60%, 80%, and 100% can only be classified as HWSCCs since their density surpasses 2600 kg/m3. The rise in density of SCC (self-compacting concrete) can be due to the greater specific gravity of barite, characterized by a size of 4–8 mm, in comparison with the natural coarse aggregate, characterized by a size of 4–8 mm.

Compressive strength at ambient temperature

The compressive strengths of SCC- mixes at 7-day and 28-day periods are illustrated in Fig. 8. For all samples, a rise in compressive strength was observed as the curing age in water progressed. The prolonged curing period resulted in specimens characterized by a dense microstructure due to hydration continuity[61,62]. Nevertheless, the compressive strength exhibited a decline as the utilization of barite as a replacement for aggregate within concrete boosted. For the reference mixture (SCC-0), the compressive strength after 7 days was 50.2 MPa. This

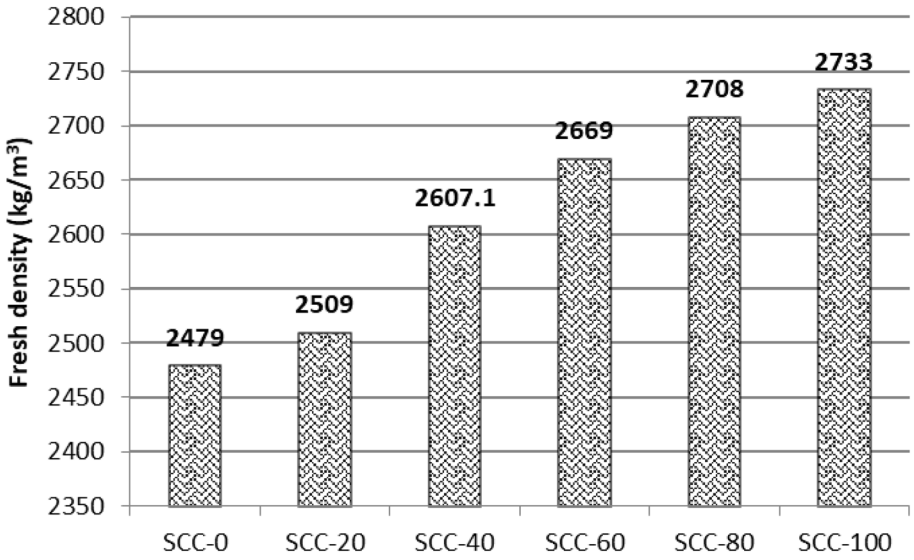

Fig. 6. Fresh density of SCC- mixtures with various barite percentages.

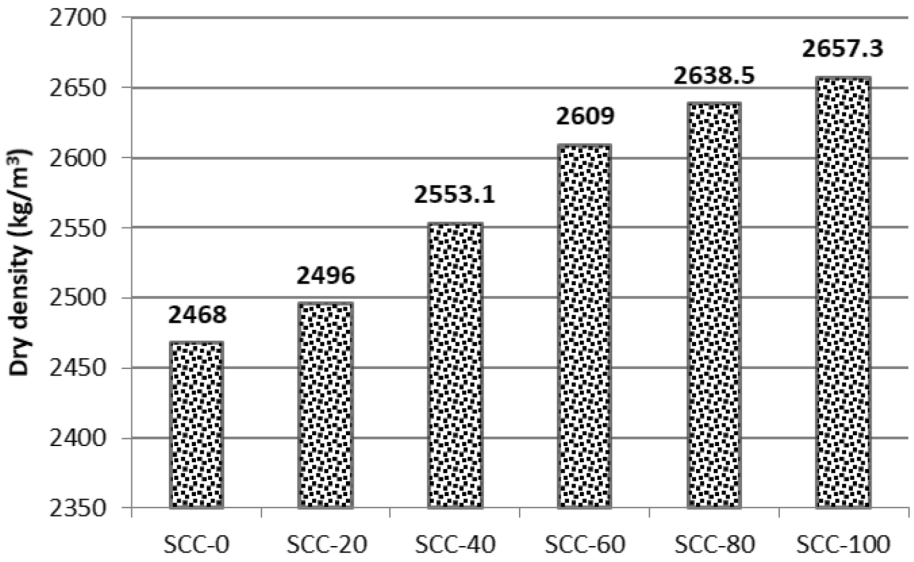

Fig. 7. Dry density of SCCs containing different ratio of barite at ambient temperature.

strength dropped by 8.78%, 5.85%, 4.88%, 4.29%, and 2.73% for blends SCC-100, SCC-80, SCC-60, SCC40, and SCC-20, respectively. The compressive strength of the reference mixture increased, reaching 67.6 MPa after 28 days. In comparison to this value, the compressive strengths of SCC blends with barite aggregate decreased by 7.39%, 5.17%, 4.73%, 2.81%, and 1.93% for SCC-100, SCC-80, SCC-60, SCC-40, and SCC-20, respectively.

Based on Bažant's investigation[58], the fracture of concrete structures results from the crack band propagation, with the width at the front being a fixed material property, approximately three times the maximum aggregate size. This could provide an explanation for the limited decline in compressive strength as the proportion of barite rises. However, the present investigation shows that the rate of strength decrease with increasing barite ratios is lower compared to prior studies[59,60]. In contrast, Bensted and Varma[61]. reported findings similar to ours. They explained that the drop in concrete's compressive strength with increasing barite proportion is due to its low toughness, which can lead to the formation of cracks directly through its grains.

Moreover, the larger water absorption for HWA aggregate in comparison with regularly weighted aggregate impedes the spread of hydrating substances. In agreement with this, an increased amount of hydration products, leading to the formation of denser C-(A-)S-H gel and a better interfacial transition zone (ITZ) within the SCC-0 blend, is illustrated in Fig. 21 and discussed in Sect. 3.5.1 and 3.5.2.

Furthermore, prior investigations have indicated that the barite aggregate in cement paste tends to increase the risk of bleeding and segregation as a consequence of the aggregate's elevated weight and water absorption[21]. When segregation and bleeding occur, voids can form near the ITZ between the heavyweight aggregates and

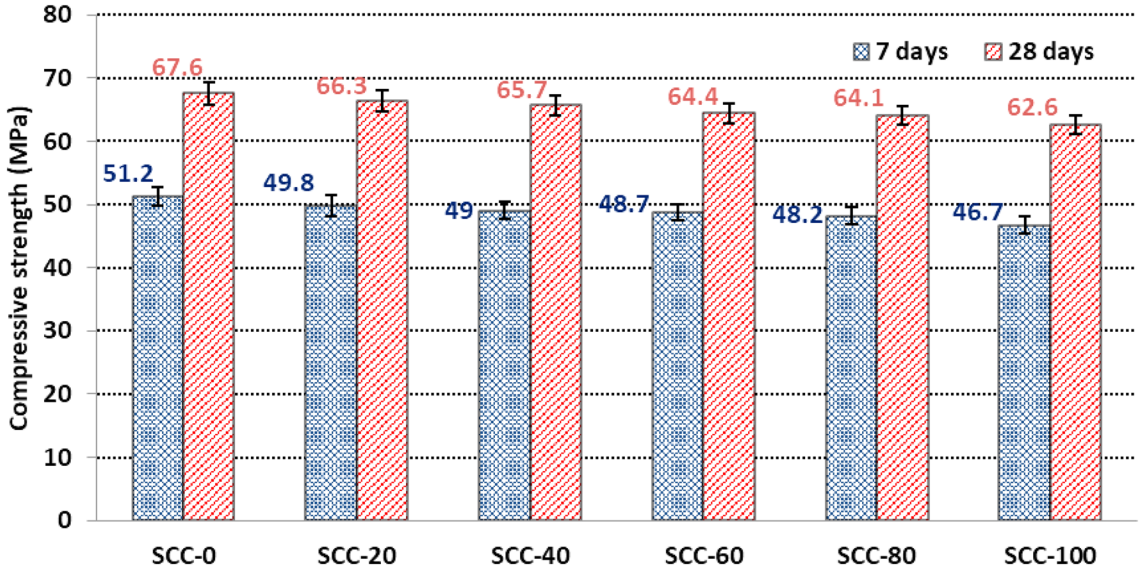

Fig. 8. Compressive strength of SCCs containing different ratios of barite at ambient temperature.

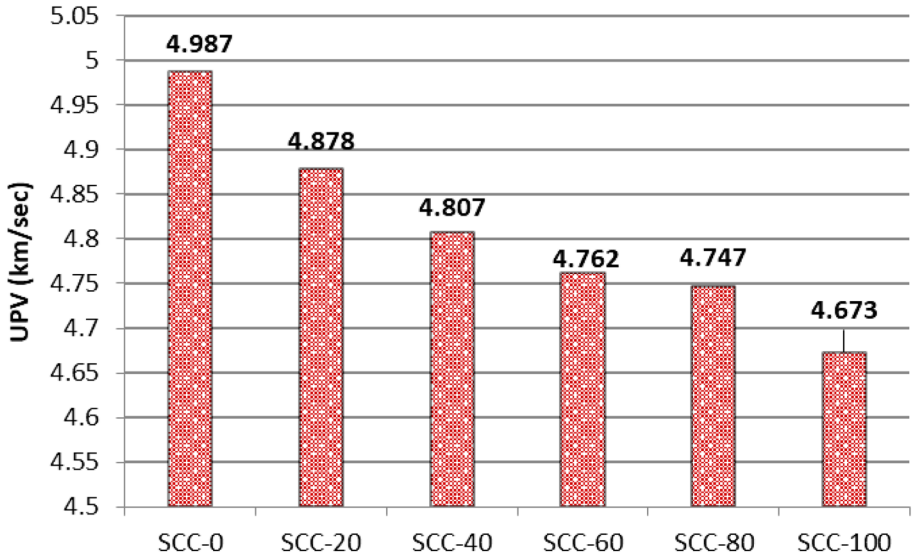

Fig. 9. UPV of SCCs- containing different ratios of barite at ambient temperature.

cement paste. The bonding between the aggregate and cement paste is weakened, resulting in a reduction in the cement paste's strength[23]. The decrease in fluidity with increasing barite content, can thus be a partial reason for the decreased compressive strength.

Ultrasonic pulse velocity at ambient temperature

Figure 9 displays the ultrasonic pulse velocity (UPV) findings of SCCwith varying barite proportions after 28 days. Based on Whitehurst's assessment[62] of concrete quality using UPV findings, the figure demonstrates that the SCCs with varying amounts of barite are of "excellent" grade. For 28 days of curing age, it was discovered that all combinations possessed outstanding performance concerning UPV. Typically, when barite is employed as a partial substitution for natural coarse aggregate (with a size of 4–8 mm), the value of UPV drops little. The highest value of UPV was detected in the reference specimen (SCC-0). A reduction of 6.29%, 4.81%, 4.51%, 3.6%, and 2.1% in UPV was observed for concrete mixtures including barite of 100%, 80%, 60%, 40%, and 20%, respectively, compared to the reference mixture. The UPV examination outcomes corroborated the findings of the compression examination, which indicated that the reference mixture exhibited the highest compressive strength. The reduction in the UPV findings for SCCs with barite content can be attributed to the decrease in stiffness and the slight rise in voids caused by the reduced hydration products, as discussed previously[58].

Mixture	After the subjection to 600 °C	CO_2-curried group	Water-curried group	Air- curing	Water glass-curing
Control					
20%					
40%					

Continued

Mixture	After the subjection to 600 °C	CO_2-curried group	Water-curried group	Air- curing	Water glass-curing
60%					

Continued

Mixture	After the subjection to 600 °C	CO_2-curried group	Water-curried group	Air- curing	Water glass-curing
80%		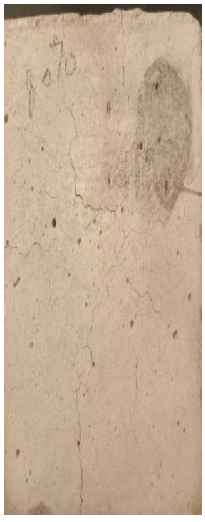			
100%					

Table 4. Heated surfaces of sccs after exposure to 600 °C and after CO_2 re-curing regimes.

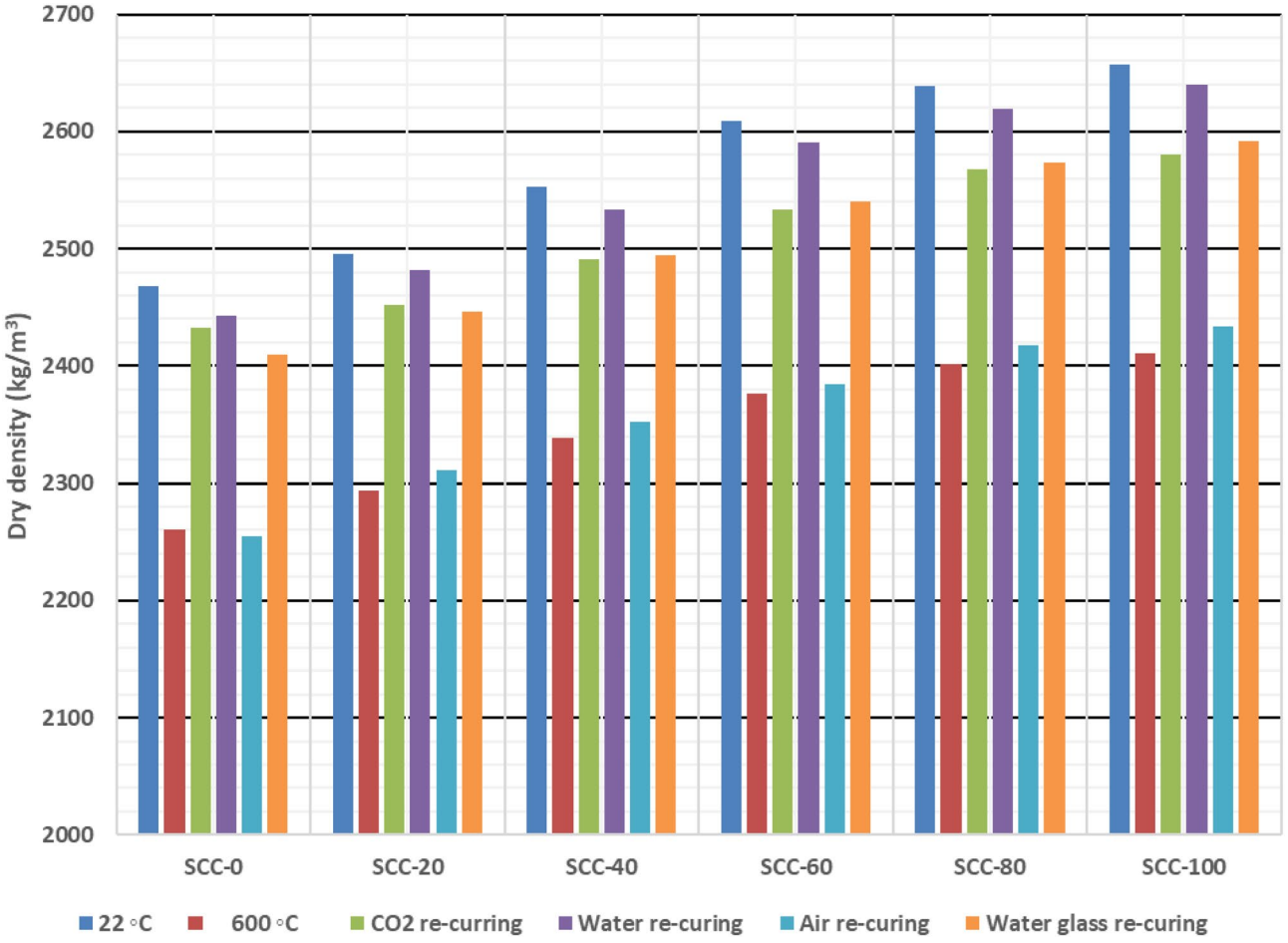

Fig. 10. Residual density for SCC- samples exposed to 600 °C and various re-curing regimes.

600 ºC exposure and re-curing regimes

Apparent properties

Table 4 illustrates the apparent characteristics of SCC following the incorporation of varying percentages of barite, after being exposed to 600 °C and subsequent re-curing treatments. Upon reaching a temperature of 600 °C, the concrete specimen underwent a change in surface colour due to chemical and physical changes, transitioning from grey to light grey. The differences in the observable characteristics of SCC-0 and SCC samples containing barite, when heated to 600 °C, varied significantly depending on the proportions of barite used (20%, 40%, 60%, 80%, and 100%). While only small cracks were observed in the SCC-0 specimens after firing, those containing heavyweight aggregate exhibited significant cracking and damage along the edges. The dimensions and amount of voids on the specimens' surface increased as the spalling of the specimens' edges progressed.

The decreased samples' thermal stability containing barite aggregate, characterized by a size of 4–8 mm, in comparison with that of reference samples with natural aggregate characterized by a size of 4–8 mm, aligns with the results of previously released research[52,53]. In their study, Luo et al.[52] recognized that concrete containing barite experiences significant spalling or scaling when exposed to temperatures beyond 300 °C (with particularly serious consequences at 450 °C). The phenomenon is mainly triggered by the barite aggregates' microfractured structure being completely or partially replaced by a limited number of heat-sensitive substances (chalcedony, quartz, and zeolites)[54–56]. Hertz[57] identified several key factors that are highly likely to contribute to the occurrence of explosive spalling in concrete structures. These factors include a high heating rate, thermal stresses, a thermal gradient, in addition to the presence of dense reinforcement and aggregate associated with low permeability, closed pores, and a moisture gradient, which includes water within the cement matrix. The significant expansion of heavyweight aggregates results in a discrepancy between the cement matrix and the aggregates, leading to the breakdown of bonds at the ITZ (interface transition zone). As a result, there is a significant propagation of microcracks inside the concrete structure[58].

Despite the evident thermal damage to SCCs with different proportions of barite exposed to 600 °C, the reparative impact of CO_2 and water re-curing is clearly visible in the photos shown in Table 4. As a result of hydration and carbonation reactions, a significant reduction in cracks and voids is observed. While re-curing of SCC samples also led to documented improvements in their surface, numerous cracks are still observed on the surfaces of samples subjected to the air-curing process. The following sections will thoroughly assess and explain the causes of these changes.

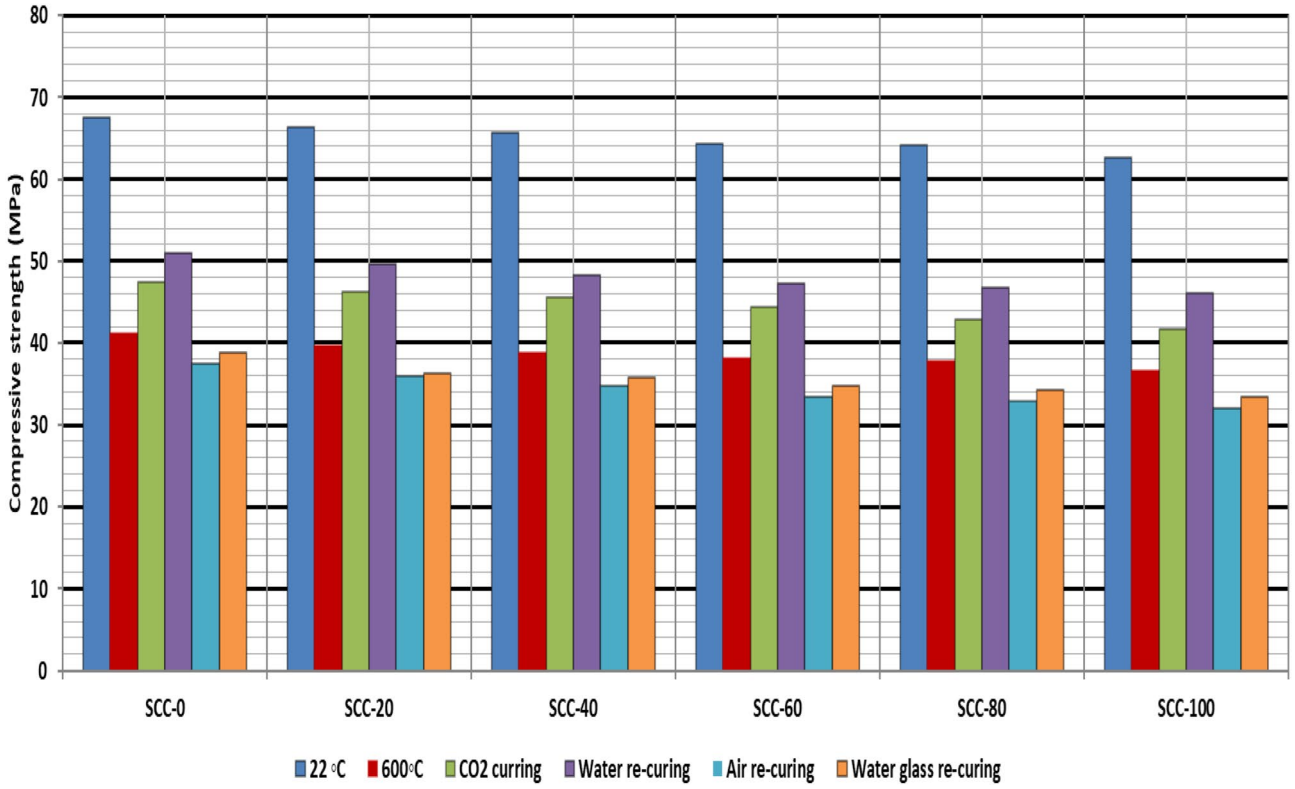

Fig. 11. Residual compressive strength of SCC samples exposed to 600 °C and various re-curing regimes.

Residual density of sccs after exposure to 600 °C and various re-curing regimes

Due to moisture evaporation, a substantial mass loss is observed in concrete with excessive humidity as the temperature increases. Therefore, the dry density decreases. Figure 10 illustrates the residual dry densities of SCCs with various barite concentrations, both before and after exposure to 600 °C, as well as after various post-fire curing regimes. Among all the SCC samples investigated, the lowest density loss (6.98%) due to exposure to 600 °C was observed in SCC-0. On the other hand, SCC-100 lost 9.29% of its density at the same temperature. In general, the density loss of SCC samples increased gradually with higher barite ratios, which relates to the physical and chemical changes occurring at elevated temperatures, as discussed previously. In addition to the disintegration of the binder structure due to the decomposition of C-(A-)S-H, CH, and other hydration products[59], SCCs containing barite aggregate also experienced spalling[52]. Furthermore, the greater water loss, resulting from the heat-sensitive substances within this heavyweight aggregate[55] and its higher water absorption compared to gravel, led to the development of microcracks. Ling et al.[28] also attributed the significant mass loss of barite-based HWC up to 300 °C to the thermal conductivity of this aggregate. Thus, the thermal stability, composition, and relative water absorption of the heavyweight aggregate regulate the density loss of HWC[24].

On the other hand, post-firing curing regimes for 28 days caused a rise within the residual dry density of the specimens, which is illustrated at Fig. 10. The highest improvement within dry density occurs in the water re-curing samples, which ultimately increased their residual dry density by 8.07%, 8.17%, 8.34%, 9.01%, 9.1% and 9.54% for SCC-0, SCC-20, SCC-40, SCC-60, SCC-80, and SCC-100, respectively, compared to the specimen exposed to 600 °C. It can be observed from the graph that the rate of increment for residual density slightly increases with increasing substitution levels of barite. This increment was due to the higher water absorption of HWA than NWA[21,24]. Another possible reason could be the refilling of fire-induced contact-type defects with water, rehydration products, and carbonated products. Park et al.[60] also demonstrated a similar water re-curing impact on the concrete density.

The increase in residual dry density values for mixtures SCC-0, SCC-20, SCC-40, SCC-60, SCC-80, and SCC-100 was 7.61%, 6.86%, 6.53%, 6.62%, 6.84% and 7.05%after CO_2 re-curing regime and 6.64, 6.63, 6.69%, 6.90%, 7.17 and 7.53% after water glass re-curing regime, respectively. This shows that the rate of improvement of dry density of SCCs at the water glass re-curing regime is slightly higher than that of the CO_2 re-curing regime samples, especially those with a high replacement ratio of barite (SCC-40, SCC-60, SCC-80, and SCC-100). The rise in residual dry density for SCC samples with 40, 60, 80, and 100% barite at water glass re-curing regime might be due to the specific gravity of water glass (1.6) as the cracks partially filled with water glass were monitored at the surface level after water glass re-curing (Fig. 20).

In terms of the results at the air re-curing regime, the density decreased slightly for SCC-0, while with increasing substitution of barite, the dry density of SCCs containing barite increased slightly. This result is consistent with the findings of Nepomuceno et al.[22]. The additional reduction in density of SCC-0 appears to be caused by shrinkage of the cement paste matrix supplied at the air re-curing regime. However, the increase

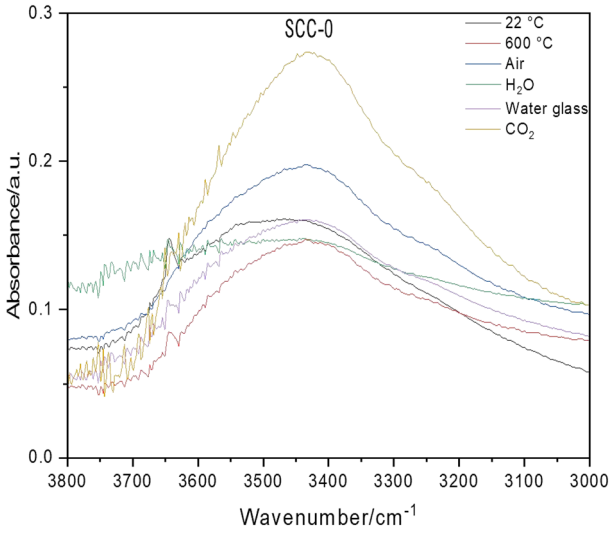

Fig. 12. Infrared spectra of SCC-0 samples before, after exposure to 600 °C, and various re-curing regimes in the O–H stretching region.

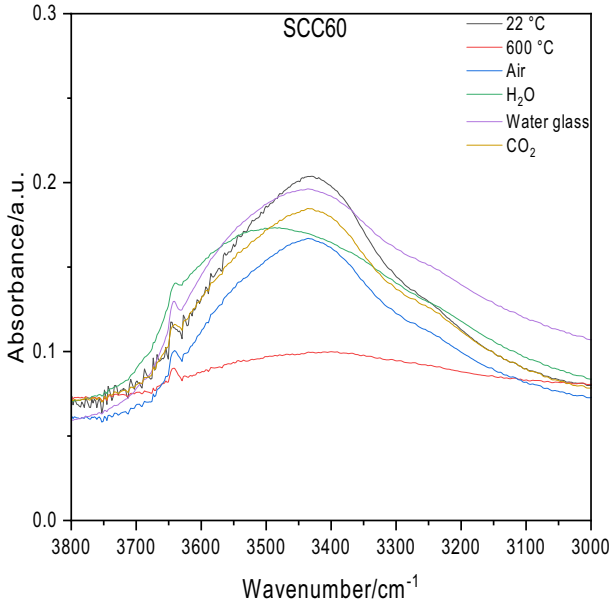

Fig. 13. Infrared spectra of SCC-60 samples before, after exposure to 600 °C, and various re-curing regimes in the O–H stretching region.

in density can be expected because of the barite's higher water absorption in comparison with gravel, which increases the mass.

Residual compressive strength (CS) of SCC after exposure to 600 °C and various re-curing regimes

Figure 11 shows the residual compressive strength (CS) of self-compacting concretes (SCCs) with different barite concentrations after being exposed to 600 °C and re-curing under various conditions. A huge drop in strength occurs because of thermal degradation which is mainly due to the breakdown of hydration products including portlandite ($Ca(OH)_2$) and calcium silicate hydrate (C–S–H), as well as the formation of internal pore pressure and microcracks.

The greatest strength recovery among all re-curing techniques was obtained with water curing. The recovery is caused by the rehydration of thermally decomposed phases. At high temperatures, portlandite decomposes into calcium oxide (CaO), and calcium-silicate-hydrate (C–S–H) gel partly breaks down. These dehydrated products experience secondary hydration when water is reintroduced, causing the regeneration of binding

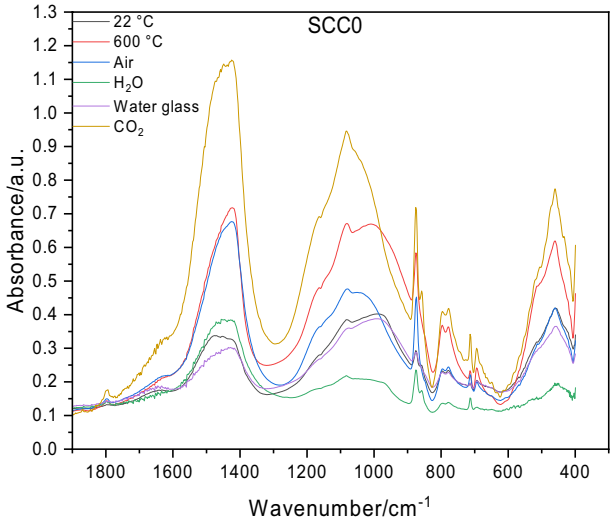

Fig. 14. Infrared spectra of SCC-0 samples before, after exposing to 600 °C and various re-curing regimes in the fingerprint region.

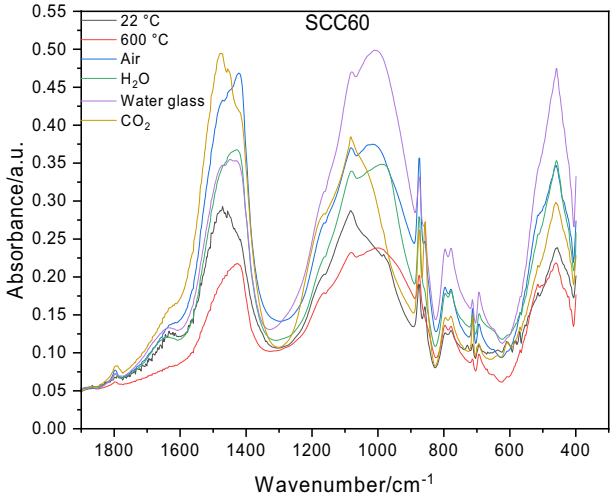

Fig. 15. Infrared spectra of SCC-60 samples before, after exposure to 600 °C, and various re-curing regimes in the fingerprint region.

Recorded vibrations/cm^{-1}	Assignment
~ 1180 (m)	$\tilde{\upsilon}_3$ (S-O) in SO_4^{2-} from barite[70]
~ 1083 (s)	$\tilde{\upsilon}_3$ (S-O) in SO_4^{2-} from barite and $\tilde{\upsilon}_3$ (Si-O) from a quarzt[71,72]
~ 988, 983 (s)	$\tilde{\upsilon}_3$ (Si-O) of Q^2 in C-(A-)S-H, $\tilde{\upsilon}_1$ (S-O) in SO_4^{2-} from barite
~ 797, 780 (w)	$\tilde{\upsilon}_1$ (Si-O) from quartz, ν(Al-OH) in $Al(OH)_6$ from AFm[73]
~ 635, 609 (w)	$\tilde{\upsilon}_2$ (O-S-O) in SO_4^{2-} from barite
~ 570, 518 (m)	$\tilde{\upsilon}_4$ (O-Si-O),
~ 460 (s)	$\tilde{\upsilon}_4$ (O-Si-O) from quartz, $\tilde{\upsilon}_4$ (S-O) from barite
~ 420 (w)	$\tilde{\upsilon}_4$ (O-S-O)[74]

Table 5. Assignments of the absorption bands and peak positions (in cm^{-1}) corresponding to Si-O, S-O, and Al-O vibrations in the MIR spectra of SCC-0 and SCC-60 before firing (δ – bending vibrations, ν – stretching). s – strong, m – medium, w – weak.

phases such as C–S–H and ettringite that facilitate mechanical recovery. The reformation of C–S–H enhances matrix density and partly repairs microcracks.

The CO_2 re-curing revealed significant strength enhancement which is mainly due to carbonation reactions. Free $Ca(OH)_2$ and even CaO in the matrix react with CO_2 to generate $CaCO_3$, which precipitates into pores, causing an improvement in the packing density and closing defects. Nevertheless, this procedure generates more brittle phases in comparison to C–S–H, resulting in worse mechanical enhancement relative to water re-curing.

On the other hand, water glass-cured and air-cured samples had limited strength recovery. The air curing was poor in moisture necessary for rehydration, whereas water glass (sodium silicate) curing, although it partially occupied pores, obstructed CO_2 penetration due to the development of a thick silicate-rich layer, leading to less stable alkali-calcium silicate hydrates ((N, C)-C–S–H). These products are often less cohesive and more fragile than traditional C–S–H, and may prevent further polymerization.

In general, the recovery processes are determined by several factors. Firstly, the water or CO_2 availability for chemical reactions with fire-degraded products. Secondly, the characteristics of the resulting phases (e.g., C–S–H against $CaCO_3$). Lastly, their ability to densify the matrix and improve interfacial transition zones (ITZ)[61].

The determined decrease in CS as the barite volume fraction increases, which is related to the loss of crystalline water from heat-sensitive materials that fill the barite aggregate micro-fractures[55]. Moreover, the poorer ITZ in the barite-containing SCCs contributes to this trend.

On the other hand, Fig. 11 shows the *CS* findings of control SCC samples with varying barite ratios, exposed to water glass, air, CO_2, and water re-curing samples. The *CS* is greatly affected by the water re-curing regime relative to other re-curing regimes. The *CS* of control SCC samples with differing barite ratios for water glass, air, CO_2, and water re-curing samples is 38.8, 37.5, 47.5, and 51 MPa, respectively, as illustrated in Fig. 11. This reveals a 15.29 and 23.78% enhancement in strength for the CO_2 and water re-curing samples, respectively, in comparison to the 600 °C sample (41.2 MPa). These findings align with the results demonstrated by He et al.[62], who revealed that water re-curing partially mitigated thermal damage, toughness, compressive strength, critical stress, and restoring the initial stress. Nevertheless, the *CS* dropped by 8.98 and 5.82% for the air and water glass re-curing samples, respectively. Furthermore, Fig. 11 illustrates that the *CS* of SCC containing 60% barite is 34.8 MPa, 33.4 MPa, 44.4 MPa, and 47.3 MPa for the samples cured with water glass, air, CO_2, and water respectively. The enhancement in *CS* was 16.53% and 24.14% for the recurred CO_2 and water samples, respectively, in comparison to the sample at 600 °C (38.1 MPa). Nevertheless, the *CS* of the recurred air and water glass samples dropped by 12.33% and 8.66%, respectively. The rate of enhancement using the recurred air and water glass regimes is clearly improved by increasing concentrations of barite. The enhancement in the *CS* of the recurred CO_2 and water regimes is due to partial recovery, since the rehydrated products occupied the voids and cracks. Throughout the period of water re-curing, the rehydration of the decomposed phases generated compounds like calcium carbonate ($CaCO_3$) and calcium silicate hydrate (C–S–H), which filled the concrete cracks. However, the regime of recurred CO_2 decreases the concrete porosity by filling voids and pores with $CaCO_3$, hence enhancing the concrete matrix densification, leading to an enhancement of residual compressive strength. At 600 °C, several hydration products within concrete, including $Ca(OH)_2$ and C–S–H, undergo decomposition. The decomposed phases may partially rehydrate and react with CO_2 during the regime of recurred CO_2, resulting in the formation of new binding phases, including supplementary C–S–H and $CaCO_3$, which leads to recovery in the strength. However, the decrease in *CS* for recurred water glass and air regimes may be attributed to the fact that air re-curing fails to offer any active physical or chemical processes to repair the damage carried out by elevated temperatures. On the other hand, recurred CO_2 or water allow

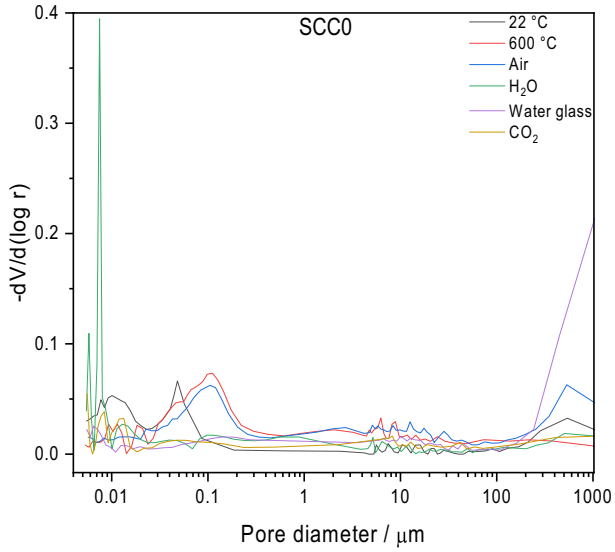

Fig. 16. Pore size distribution curves for SCC-0 samples before, after exposing to 600 °C and various re-curing regimes.

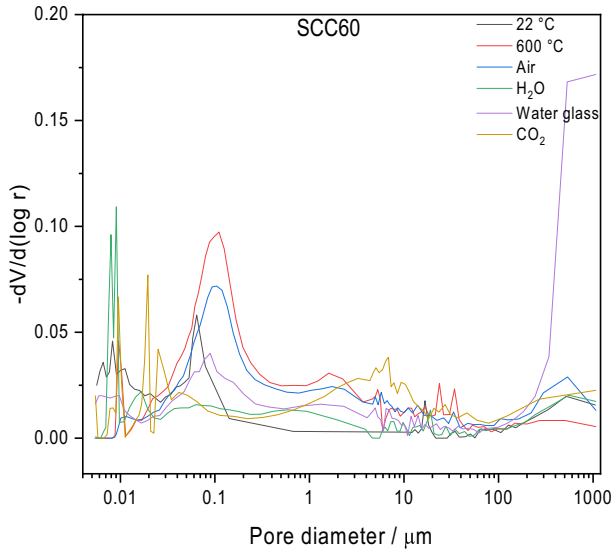

Fig. 17. Pore size distribution curves for SCC-60 samples before, after exposing to 600 °C and various re-curing regimes.

MIX ID	Curing	Pore size distribution / vol%			
		$>10^4$ nm	10^2–10^4 nm	50–10^2 nm	< 50 nm
SCC-0	22 °C	30	10	12	48
	600 °C	19	38	25	18
	Air	36	33	17	14
	H_2O	20	28	9	43
	Water glass	72	18	4	6
	CO_2	35	29	10	26
SCC-60	22 °C	26	10	21	43
	600 °C	13	43	30	14
	Air	24	43	23	10
	H_2O	32	26	11	31
	Water glass	61	20	9	10
	CO_2	31	43	6	20

Table 6. Pore size distribution (The amount of pores within the specified region of pore diameter) of SCC-0 and SCC-60 specimens.

carbonation or rehydration, where recurred air depends exclusively on natural processes that are inadequate for restoring lost hydration products or repairing microcracks. Regarding the decrease in compressive strength due to water glass, recurred sodium silicate, often known as water glass, may react with calcium compounds within concrete to produce C–S–H. Nevertheless, these newly generated phases could show reduced stability or increased brittleness relative to the original hydration products, resulting in decreased strength. Furthermore, while water glass may partially occupy pores and cracks, it does not adequately restore the original bonding structure of the concrete. The newly created phases might not incorporate well with the current matrix, resulting in a weakened overall structure. The current results concerning water curing surpasses CO_2 curing aligns with the findings of Onyelowe et al.[45] and Bouhafs et al.[46], who ascribed recovery to rehydration processes and the reformation of C–S–H, as opposed to the brittle precipitation of $CaCO_3$. The research conducted by Song et al.[63] demonstrates that slag-modified cements significantly diminish microcracking during rehydration, which leads to an improved residual mechanical performance.

FTIR analyses

MIR spectra of the specimens are shown in Figs. 12, 13, 14 and 15. Between 3750 and 3050 cm^{-1}, very broad absorption bands with the maxima at approximately 3400 cm^{-1} due to stretching vibrations from water and OH species adsorbed on the surface occur (Figs. 12, Fig.13). Corresponding OH bending vibrations appear between 1750 and 1600 cm^{-1} with maxima located around 1630 cm^{-1} (Figs. 14 and 15). While firing the samples led to the loss of structural and physically adsorbed water, subsequent curing ensured the reintegration of water into the structure.

The sharp absorption band of weak intensity observed at approximately 3640 cm^{-1} might be attributed to the O–H stretching vibration of $Ca(OH)_2$, and in the case of samples before firing may overlap with that of ettringite[62]. As shown in Fig. 12, the highest intensity of the particular band is observed in the sample without barite addition before firing. Partial decomposition of portlandite by heating the concrete samples at 600 °C resulted in a decrease in intensities. The disappearance of this band in the MIR spectra of samples without barite, exposed to CO_2 and air curing, is caused by a carbonation reaction. In contrast, portlandite is still present in all the samples prepared with 60% barite (Fig. 13).

As indicated by the strong and broad absorption bands belonging to the asymmetric stretching ῡ3(CO) (between 1600 and 1300 cm^{-1}) and two less intense bending ῡ2 (OCO) and ῡ4 (OCO) (between 890 and 700 cm^{-1}) vibrations of the carbonate ion (Figs. 14 and 15), pronounced carbonate formation was achieved under post-firing treatment regimes[64,65]. Accelerated carbonation is a result of the high porosity of the samples generated during firing. The formation of calcium carbonates with varying degrees of structural disorder, as well as the presence of the calcite´s deformation vibrational modes (out-of-plane bend at 876 cm^{-1} and in-plane bend at 713 cm^{-1}), is confirmed based on the appearance of corresponding absorption bands[66]. Furthermore, the presence of other characteristic bands at about 858 and 693 cm^{-1} indicates that a second polymorphic form of $CaCO_3$ (aragonite), in addition to calcite, is present in some samples[67,68]. Only stable calcite was observed in the samples after exposure to 600 °C.

The areas in the MIR spectra, which are below 1300 cm^{-1} are characterized by S-O and Si-O vibrations (Figs. 14 and 15) showing two strong and broad complex absorption bands. The first band, located in the range 1200–900 cm^{-1} which could be attributed to the Si-O and S-O asymmetric ($\tilde{\upsilon}_3$) and symmetric ($\tilde{\upsilon}_1$) stretching vibrations and a second group of bands in the range 600–400 cm^{-1} with maxima at about 460 cm^{-1} corresponding to O-S-O and O-Si-O bending vibrations ($\tilde{\upsilon}_4$ and $\tilde{\upsilon}_2$)[69]. The main Si-O and S-O stretching and bending vibrations observed in SCC-0 and SCC-60 before firing are detailed in Table 5. In addition to the absorption bands from the barite aggregate structure, a significant difference within the Si-O asymmetric stretching vibrations region associated with C-(A-)S-H hydration phases can be observed between the MIR spectra of the SCC-0 and SCC-60 samples. The wide, intense band peaking around 988 cm^{-1} in the spectrum of SCC-0 indicates the formation of a more disordered and polymerized structure of C-(A-)S-H gel. On the contrary, the absorption spectrum of SCC-60 exhibits a much less intense but sharper peak located at 983 cm^{-1}. This, in line with the previously discussed results, indicates restricted hydration and pozzolanic reactions due to hindered water penetration and lower temperatures caused by the presence of barite aggregate.

Considering absorption bands below 1300 cm^{-1}, the main changes caused by firing and post-firing treatments in both compositions are recorded within the Si-O stretching vibrations area. The partial decomposition of C-(A-)S-H phases into C_3S and C_2S following the firing of concretes at 600 °C can be inferred from the shift of the maxima, previously observed at 988 and 983 cm^{-1}, as well as the broadening of the corresponding bands toward lower wavenumbers. This is consistent with the positions of the bands referenced in[75] and the findings of other studies[76–78]. Simultaneously, the absorption band intensity around 518 cm^{-1}[79], linked to O-Si-O vibrations caused by C_3S out-of-plane bending, increased.

Following the post-firing treatment, the maxima corresponding to Si-O stretching vibrations shifted toward higher wavenumbers. Regardless of the presence of barite, the most significant shift was observed in samples processed in a CO_2 chamber, followed by air-recured SCCs. Both the rehydration of C_3S and C_2S, causing C-(A-)S-H decalcification, besides the formation of polymerized C-(A-)S-H phases due to carbonation and its subsequent polymerization, would cause such changes. More pronounced carbonation is observed in both samples mentioned.

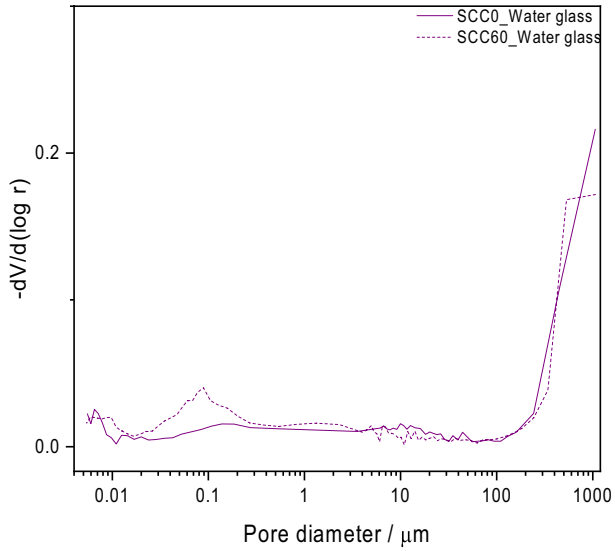

Fig. 18. Pore size distribution curves for SCC-0 and SCC-60 after water glass curing.

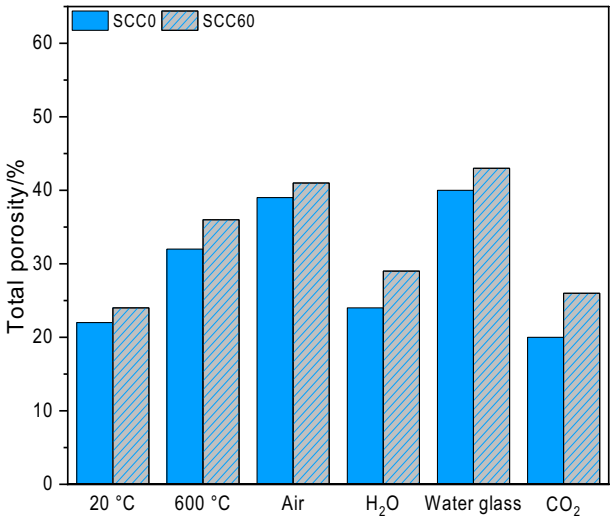

Fig. 19. Values of total porosities of SCC-0 and SCC-60 samples determined by MIP.

On the contrary, in line with the absorption bands resulting from the stretching and bending vibrations in CO_3^{2-}, the samples immersed in water glass were less carbonated. According to SEM-EDX mapping (Fig. 21), the inhibition of the carbonation process resulted from the formation of a dense, silicate-rich layer on the surface of SCC samples, which restricted CO_2 diffusion into the material. A significant shift of the absorption band from Si–O stretching vibrations in SCC-60 processed in water glass towards higher wavenumbers is not caused by pronounced rehydration but by the emergence of amorphous Si-O stretching vibrations originating from the amorphous water glass[80]. The less pronounced presence of sodium silicate solution in SCC-0 after treatment with water glass can be attributed to a more compact pore structure (Fig. 7), resulting from the initial formation of a greater amount of hydration products.

In SCCs post-treated with water, both carbonation and the reformation of the largest quantity of hydrated C-(A-)S-H phases are evidenced through absorption spectra and supported by the highest compressive strength values among the post-treated specimens (Fig. 8). In addition to the observed shift of the band from Si-O stretching vibrations, the most pronounced rehydration of these samples is confirmed by the decreased intensity of the band at approximately 518 cm^{-1} compared to that of in-plane vibrations (~ 460 cm^{-1}). This reduction reflects a decrease in the freedom of motion associated with the formation of polymerized C-(A-)S-H.

Microstructural analyses

MIP analysis

Figures 16 and 17 illustrate the results of the MIP analysis for the SCC-0 and SCC-60 samples, presented as pore size distribution curves. Table 6 summarizes the "pore size distribution" (the portion of pores within a given diameter range) of the samples based on the classification of pores according to Mehta and Monterio[81]. It is important to note that the term "pore sizes" refers specifically to the percolation size of pores corresponding to the intruded pressure only. One should also be aware of the limitations of the MIP technique that may influence the following results [e.g.[82,83]].

The lower detection limit of the device used did not allow for the determination of pores with diameters below 3.5 nm, which could be classified as gel pores. Nevertheless, as shown in the curves (Figs. 16 and 17) and in Table 5, both SCC-0 and SCC-60 before firing contain the highest percentage of pores with dimensions below 50 nm (48 and 43%, respectively), which can be classified as small capillaries. It indicates the compact microstructure of the prepared SCC samples, as confirmed by SEM (Fig. 20) and compressive strength measurements (Fig. 8). The determined total porosity values are 22 and 24%, respectively. This, along with the percentage of the smallest pores present in these samples, confirms a slightly restricted hydration of SCC-60 due to the presence of barite aggregate.

Following firing at 600 °C, which resulted in the loss of chemically bound water and partial loss of CO_2, the proportion of smaller pores decreased. In contrast, the proportions of medium (pores with diameters between 50 and 100 nm) and large capillaries (pores with diameters between 10^2 and 10^4 nm) increased significantly. Li et al. also recorded a similar bimodal pore size distribution in concrete exposed to 600 °C[84]. The left-hand peaks are associated with the decomposition of hydration products leading to the coalescence of pores, while the right-hand peaks correspond to the formation of microcracks observed via SEM (Fig. 20).

The MIP results for post-firing treatments are consistent with those from FTIR and mechanical testing. The most significant microstructure refinement (Figs. 16 and 17; Table 5) was achieved by using the water curing method followed by CO_2 treatment of the SCCs. The largest changes observed in both post-firing treatment processes were in the portion of small capillaries, with a smaller decrease in the portion of large capillaries. This is expected, as rehydration and carbonation primarily occur within small capillaries, which provide a higher surface area relative to volume, facilitating more efficient interaction with water and CO_2. Additionally, $CaCO_3$

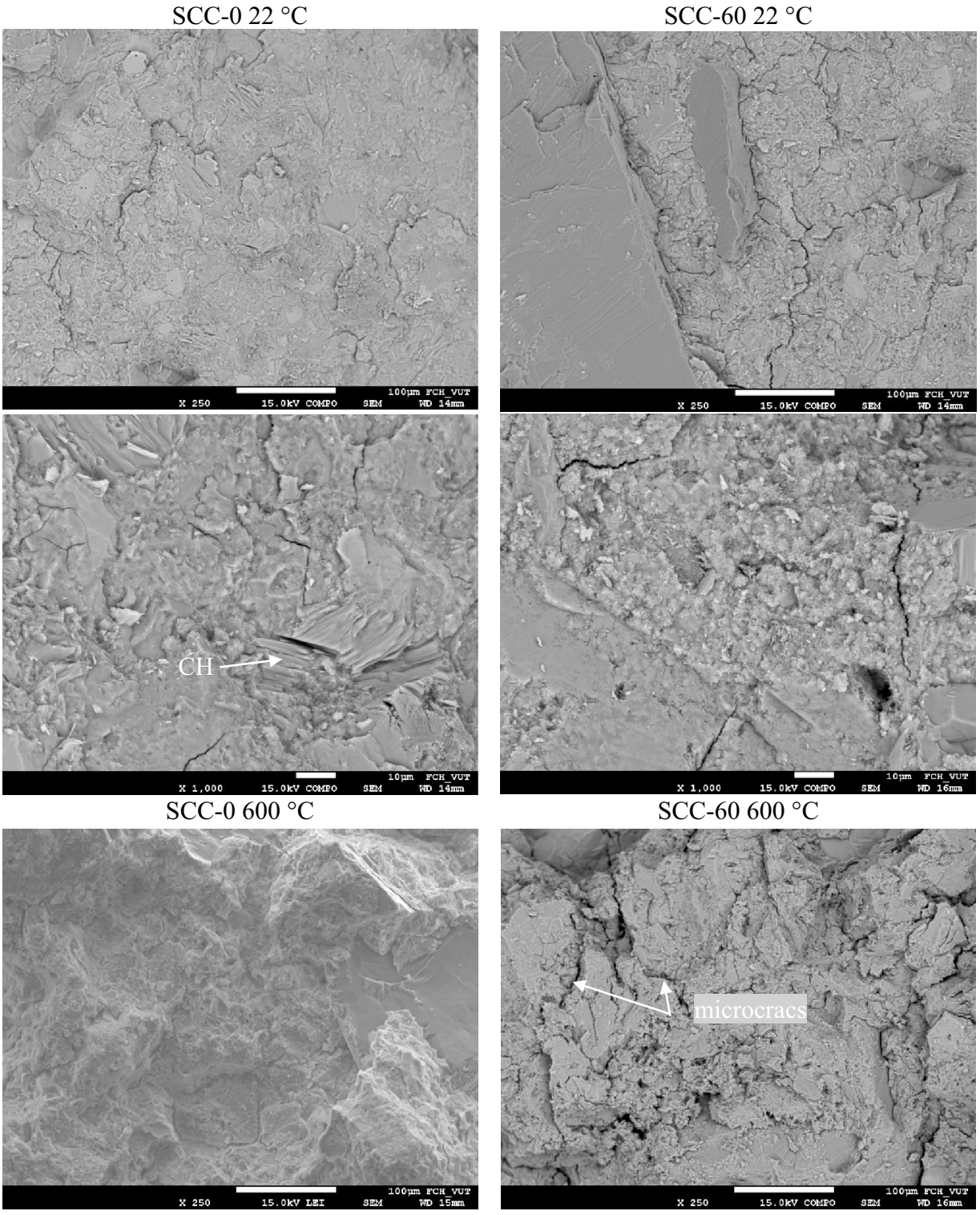

Fig. 20. Microstructure of the fracture surface of SCC-0 (left) and SCC-60 (right) samples, shown before firing, after firing, and following different post-firing treatments.

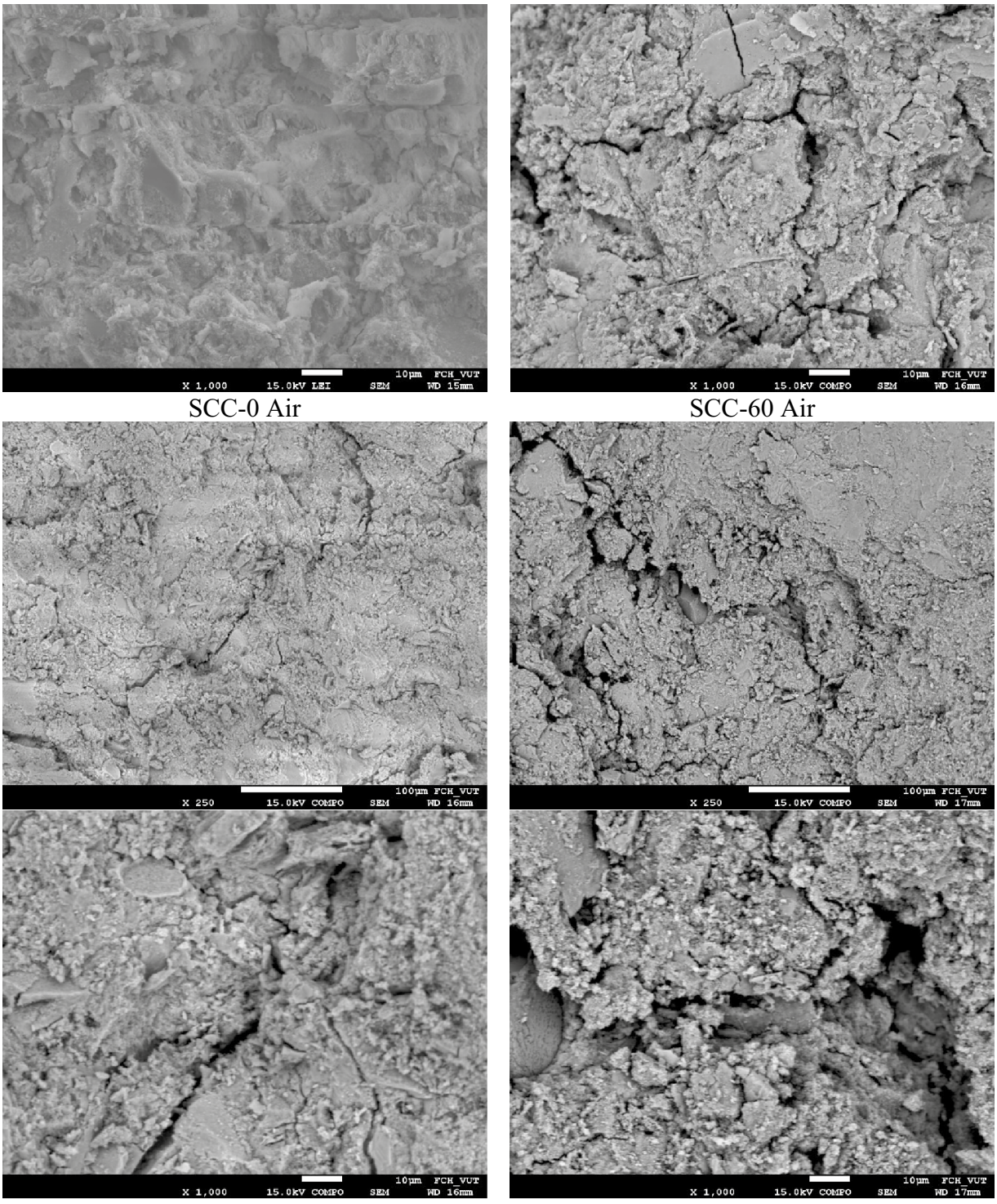

Fig. 20. (continued)

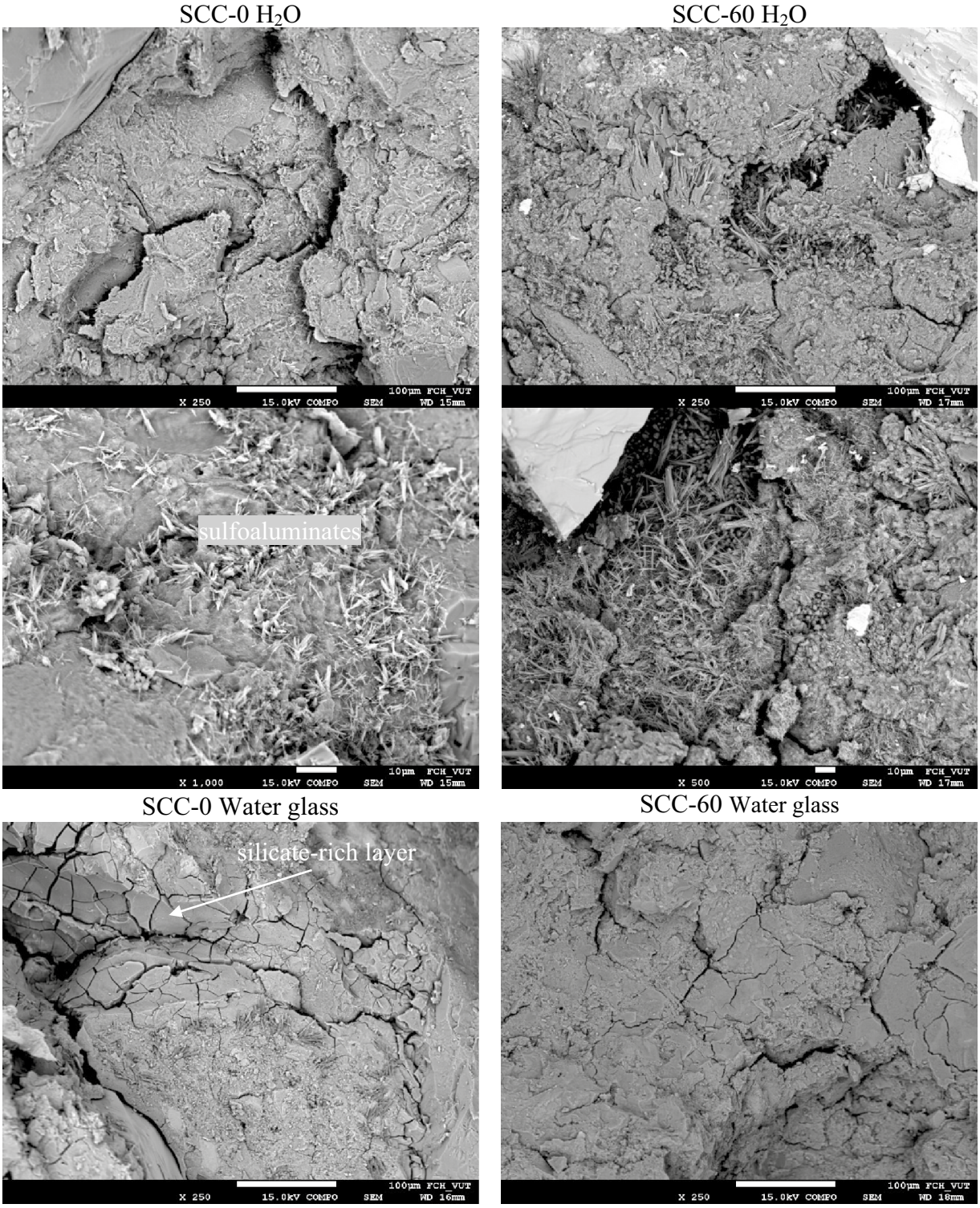

Fig. 20. (continued)

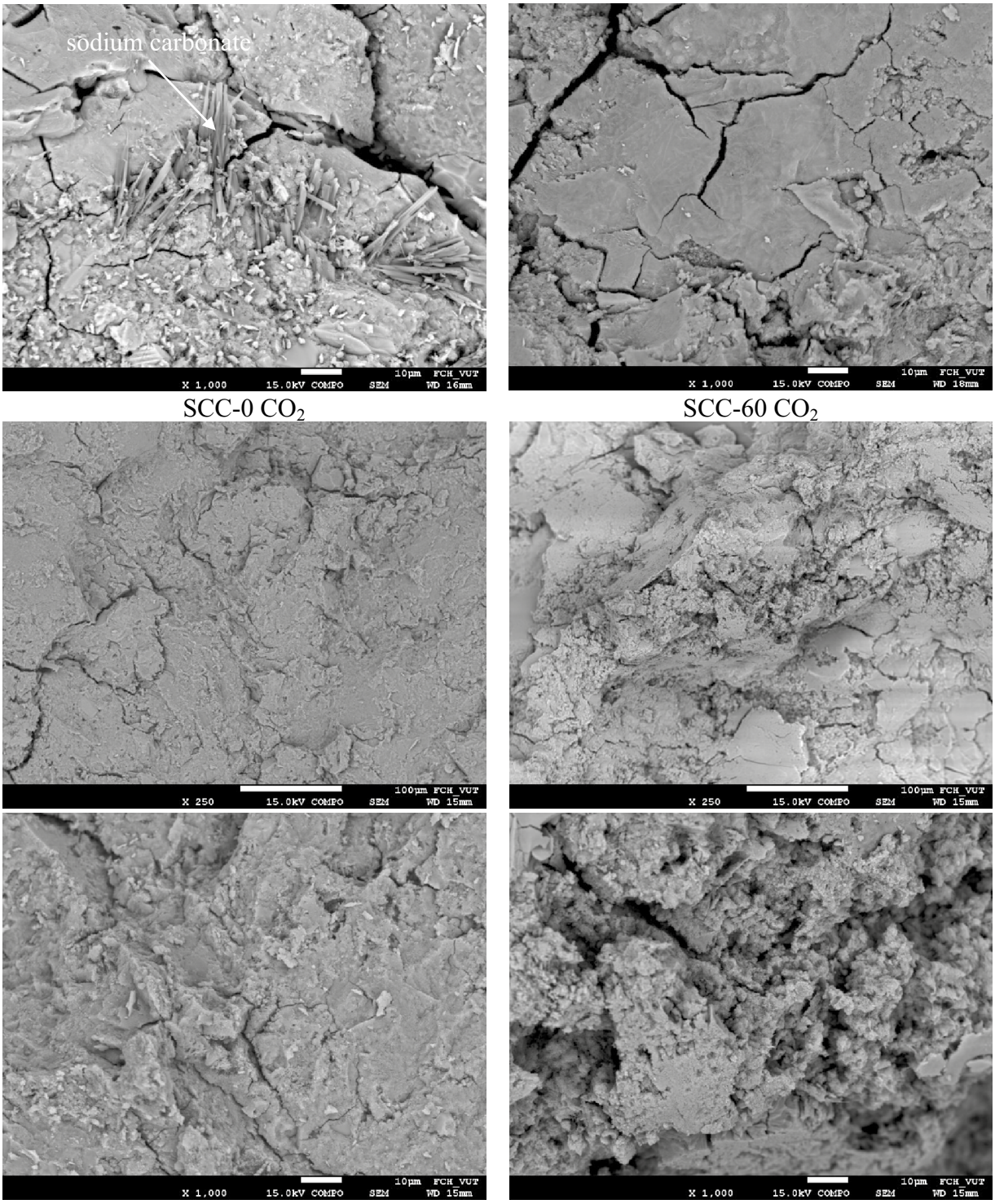

Fig. 20. (continued)

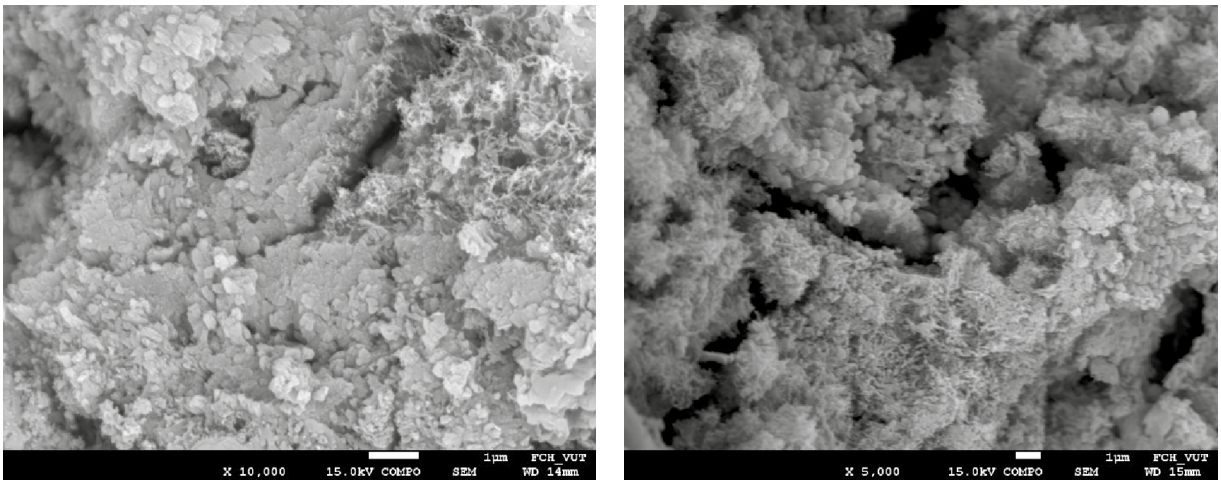

Fig. 20. (continued)

precipitation tends to occur preferentially in smaller pores due to better water condensation[85]. The greater effectiveness of water curing is due to a larger rise in the volume of rehydrated phases in comparison with the pore-filling effect of calcium carbonates formed by reactions with CO_2. Additionally, for carbonation to occur in concrete, CO_2 must dissolve in water to form carbonic acid, which then reacts with calcium ions from C_3S and C_2S, as well as with other still-hydrated phases, to produce $CaCO_3$. When pore water is limited post-firing, carbonation is restricted since insufficient water is available to dissolve CO_2 and facilitate reactions with calcium silicates, thereby reducing the effectiveness of CO_2 treatment.

Unlike the water and CO_2 post-firing treatments, re-curing SCCs in air and water glass was not beneficial. The total porosity values (Table 6(and pore size distribution curves (Fig. 16) determined by MIP confirmed further pore structure coarsening compared to the samples after firing. The primary reason for the failure of the air re-curing regime is drying shrinkage, which leads to the formation of microcracks. Increased microcracking was confirmed through surface photos (Table 3) and SEM analysis (Figs. 20 and 21). Additionally, although significant carbonation of SCC samples left to re-cure in the air was demonstrated by FTIR (Figs. 14 and 15), the resulting calcium carbonates primarily act as fillers and do not provide the bonding strength that rehydrated C-(A-)S-H phases offer under a water re-curing regime. Carbonation of unhydrated calcium silicates produces silica gel, which has a lower volume compared to hydrated phases. Moreover, after the total consumption of portlandite, as observed in SCC-0 (Fig. 12), the pH decreases to below 11, leading to the formation of water-soluble calcium hydrogen carbonate $\left(Ca(HCO_3)_2\right)$, which easily diffuses out of the cement matrix[86]. These factors collectively contribute to the observed increase in porosity. The deterioration of microstructure, leading to weakened strength characteristics in air re-cured concrete samples, was also observed in[87]. The refinement of microstructure and improvement in compressive strength achieved through CO_2 post-firing treatment, as opposed to air treatment, is due to the higher humidity in the CO_2 chamber, which facilitated both carbonation and hydration reactions. On the other hand, the ambient relative humidity was 50%, which was unsuitable for enabling huge hydration processes, resulting in a deterioration in microstructure and a reduction in the strength.

For SCC samples exposed to water glass, coarsening of the pore structure occurred despite partial rehydration of calcium silicates, with the alkali content from the water glass likely contributing to the formation of alkali-calcium silicate hydrates ((N, C)-(A-)S-H). One contributing factor is the inhibition of carbonation due to the formation of a silicate-rich surface layer, as previously discussed. The slower hydration reactions within the concrete compared to water curing may also be attributed to the high viscosity of water glass, which restricts ion diffusion. Additionally, the deterioration in pore structure and related decline in mechanical properties may result from the high sodium silicate modulus ($M = SiO_2/Na_2O$) and alkali content (Na_2O) (Table 4). As demonstrated in[88], excessive alkalinity can cause silico-aluminate oligomers to decompose into separate aluminum and silicate ions, reducing oligomer content and hampering polymerization.

The highest proportion of macropores and the lowest proportion of capillaries in SCC samples immersed in water glass (Fig. 18; Table 5) can be attributed to insufficient drying techniques that failed to remove unreacted water glass (as confirmed by FTIR), likely due to its high viscosity, particularly in smaller pores (Fig. 19). Additionally, the outer silicate-rich layer may have trapped residual internal stresses, leading to the generation of microcracks, as also observed in (Figs. 20 and 21).

SEM analysis

The microstructure of the fracture surfaces in SEI mode and the cross sections in BSE mode for all investigated SCC samples are shown in Figs. 20 and 21, respectively.

The more compact microstructure of SCC-0 before firing, with a higher proportion of crystalline products (such as portlandite with hexagonal platelet morphology), results from its greater degree of hydration, as discussed previously. Correspondingly, BSE images of SCC-60 reveal a higher content of bright anhydrous clinker grains. The increased presence of microcracks in SCC-60 is due not only to restricted hydration but also

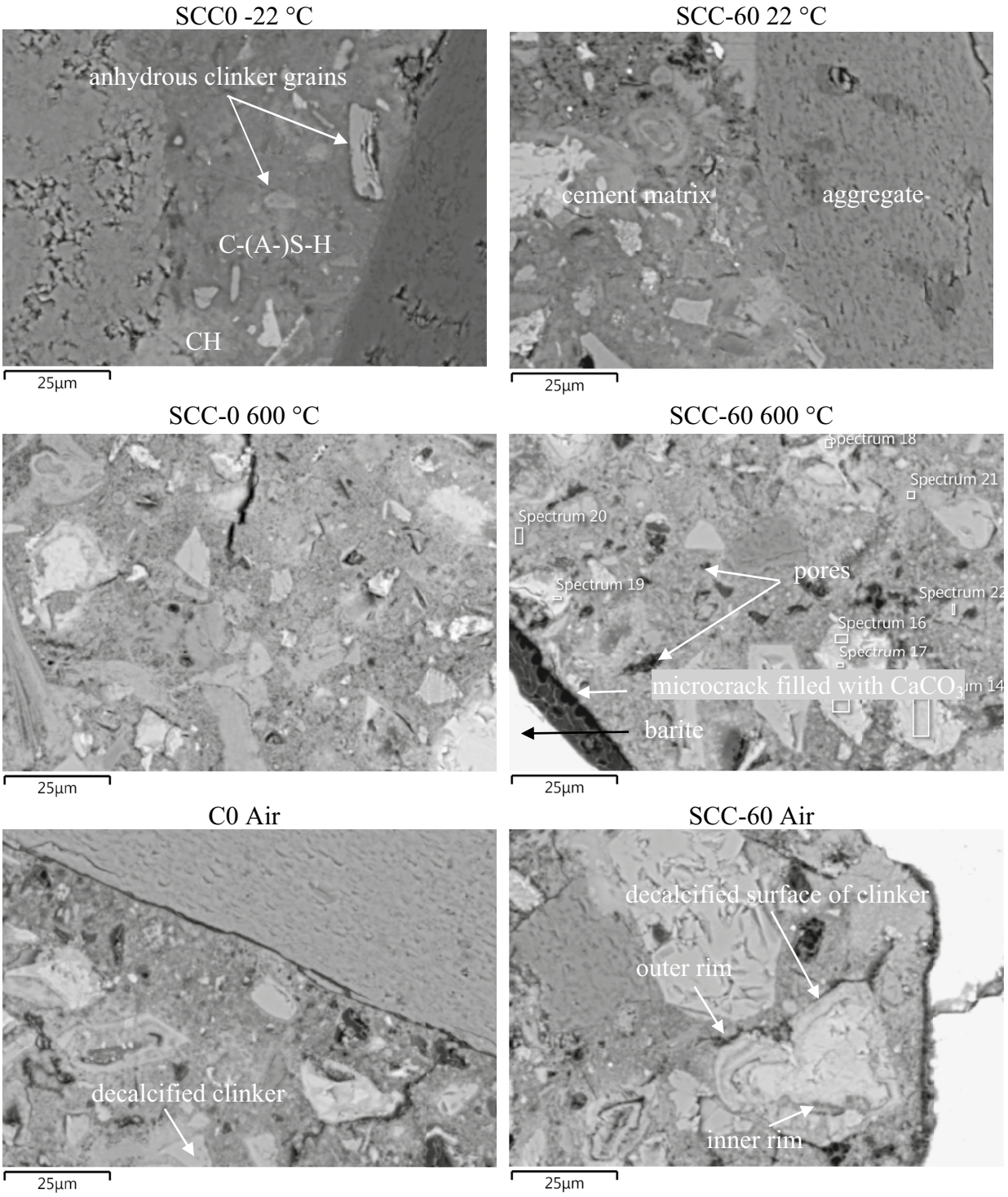

Fig. 21. SEM-BSE images of SCC-0 (left) and SCC-60 (right) samples.

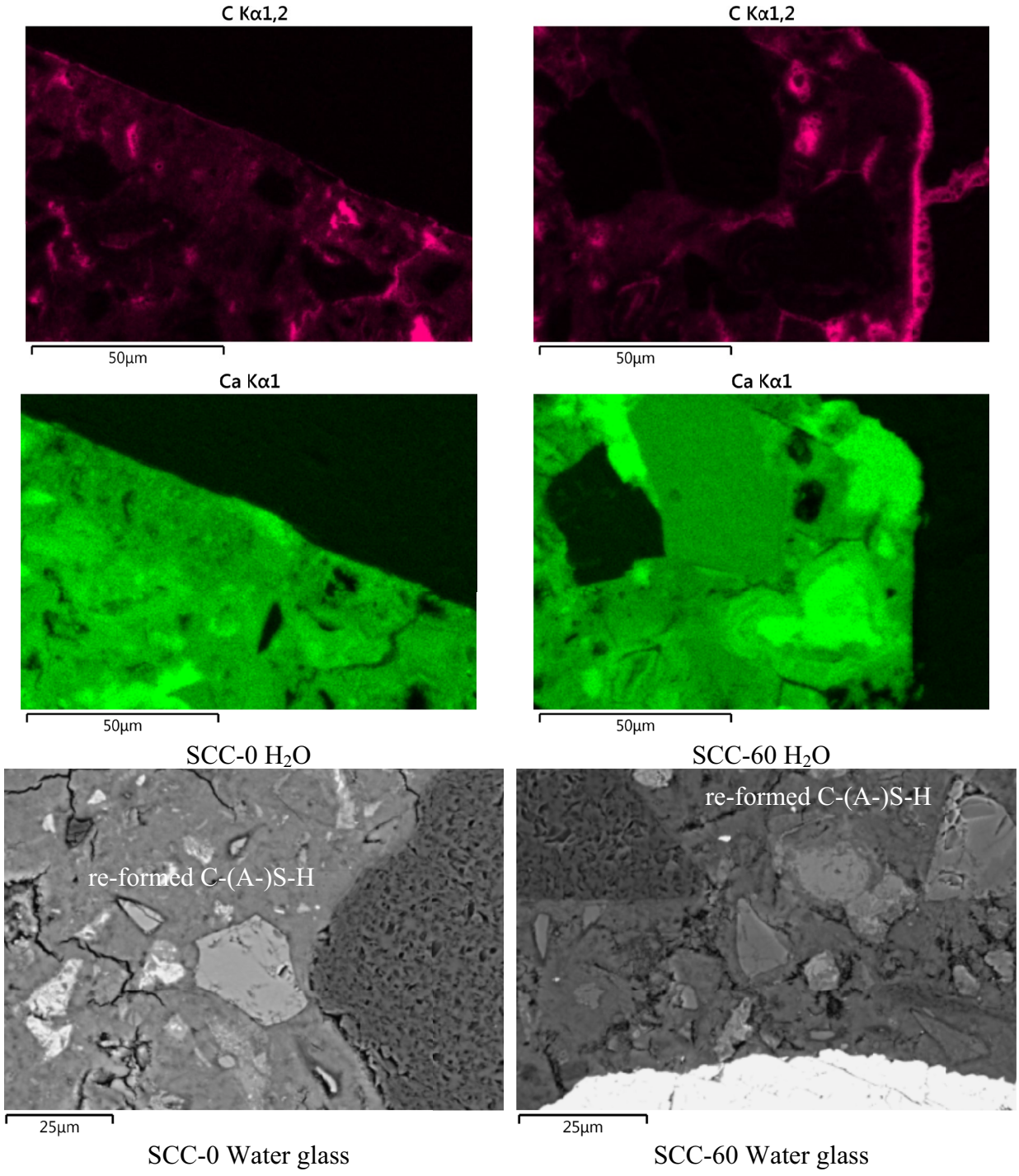

Fig. 21. (continued)

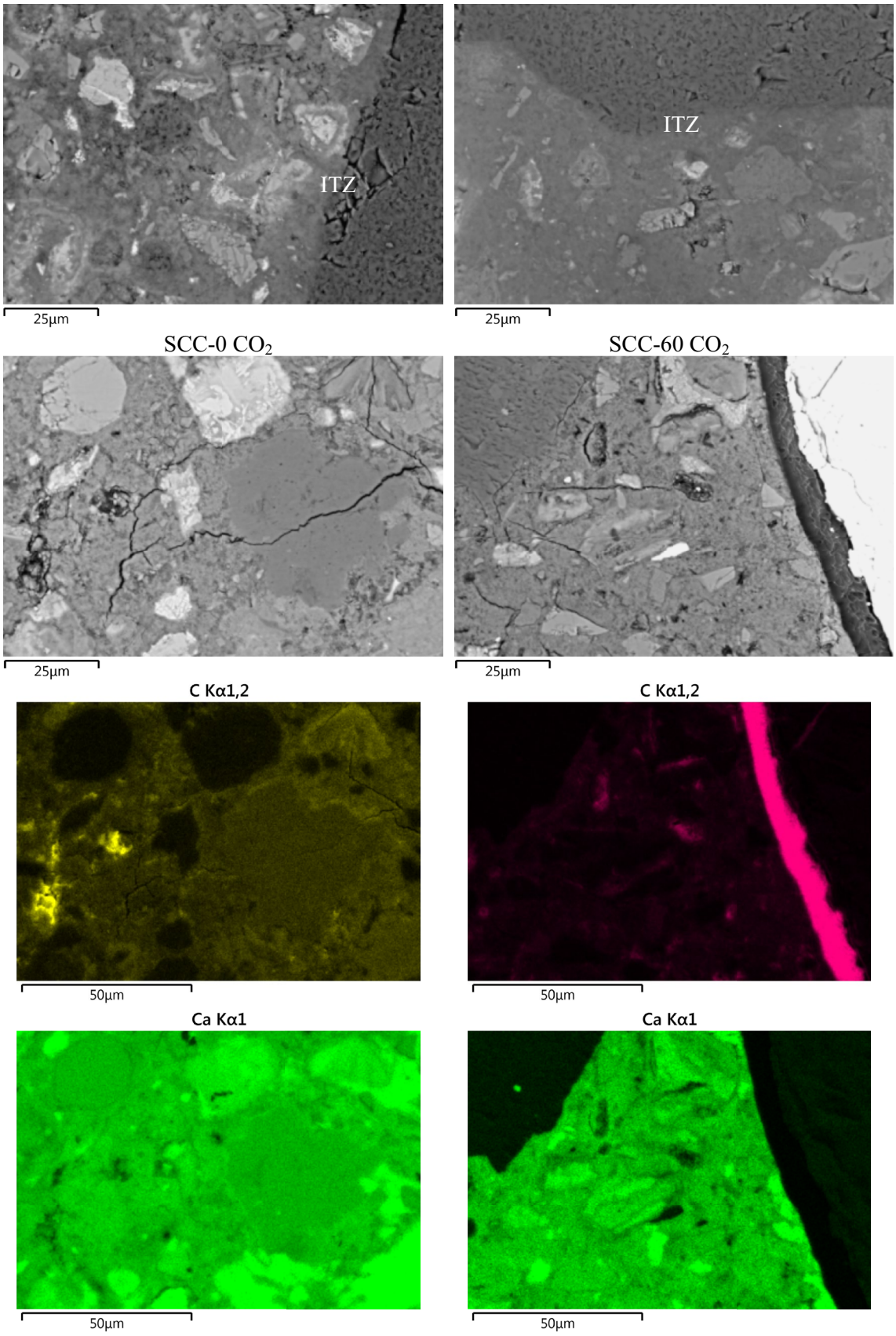

Fig. 21. (continued)

to more significant drying shrinkage, which results from moisture distribution affected by the presence of barite, and a weaker ITZ between the barite and cement matrix.

Subjecting the samples to 600 °C significantly affected their microstructure. Crystalline hydration products disappeared, and the microstructure became more amorphous, appearing even granular in the case of SCC-60. The greater internal stresses in this sample resulted in a higher occurrence of microcracks and pores (black in BSE). Visualization in BSE mode confirmed the loss of chemically bound water from hydrates, indicated by an increase in brighter areas compared to the darker grey levels of AFm phases and C-(A-)S-H, ettringite[89], .

In accordance with the results of MIP and measured compressive strength values, re-curing the samples in air led to a more pronounced formation of microcracks and pores. Cracks preferentially formed along the aggregate boundaries. The presence of wider microcracks along barite grains (white in BSE) and within the binder matrix in SCC60 aligns with the observed higher proportion of large capillaries. Increased porosity in air-cured samples was also a result of decalcification of clinker grains due to carbonation, as documented by images in BSE mode and the attached EDX maps. In the image of the corresponding SCC-60 sample, two distinct rims around the clinker grains are visible. The brightest region corresponds to anhydrous cement grains, the darker rim to the decalcified area, and the light grey region to calcium carbonates precipitated during carbonation, intermixed with decalcified C-(A-)S-H or silica gel[90].

SEM images of water glass-cured samples demonstrate numerous microcracks, which are consistent with MIP findings. As suggested earlier, reactions leading to the improvement of the microstructure and related mechanical properties were hindered by the presence of a glassy, silica-rich layer in the surface of these samples, which is visible in (Fig. 20). However, in contrast to air-cured samples, a larger portion of rehydrated phases (darker grey areas in BSE), as well as an improved ITZ, can be observed (Fig. 21), corresponding to higher compressive strength values. The recorded C-S-H regrowth corresponds with the findings of Wang et al.[90], demonstrating the significance of rehydration in microstructural repair. Furthermore, carbonation in the presence of sodium silicate solution caused sodium carbonate crystals formation with a needle-like morphology (Fig. 20).

Images of SCC samples after water curing, captured in both SEI and BSE modes, reveal a significant amount of rehydrated amorphous and crystalline phases, which contributed to the refinement of the microstructure, as confirmed by MIP. Elongated, fibrous crystals preferentially filling pores and cracks are likely re-hydrated sulfoaluminates[91].

The densified microstructure of SCC samples re-cured in the CO_2 chamber is shown in Fig. 20. The microcracks appear narrower compared to those in other post-firing treated samples, and both the microcracks and pores are filled with carbonation products (Fig. 21). Short, rod-shaped crystals were identified as calcite[16,22], while finer precipitates are likely aragonite, the most significant presence of which was confirmed in these samples by FTIR analysis (Figs. 14 and 15). Additionally, the humidity in the chamber facilitated the regeneration of C-(A-)S-H with a network-like microstructure, which contributed to the enhancement of the mechanical properties.

Conclusions

The present research offers comprehensive insights on the impact of different post-fire re-curing regimes (water glass, air, CO_2, and water) on the compressive strength recovery within thermally damaged SCC samples incorporating barite to replace coarse aggregate with a size ranging from 4 to 8 mm at varying percentages (20–100% at 20% intervals). The examination utilized FTIR, MIP, and SEM to examine alterations in pore size distribution, porosity, microstructure, and phase assemblage of the SCC samples with varying barite percentages, subjected to 600 °C and treated in diverse post-fire re-curing regimes. According to the results and discussion mentioned above, the following conclusions can be drawn:

- The exposure of SCC mixtures to 600 °C resulted in significant physical changes, including a decrease in density around 9%, a loss in compressive strength of 30–45%, and a rise in porosity, besides more severe deterioration at higher barite levels of substitution.
- The deterioration was mostly due to the breakdown of hydration products (C–S–H, CH, ettringite), microcracking in the interfacial transition zone (ITZ), and spalling of barite-rich concretes.
- Post-fire re-curing regimens significantly affected the recovery trend. Water re-curing facilitated rehydration and regeneration of C–S–H, which resulted in a restoration of compressive strength to 75% of its original value and enhancing the pore structure.
- CO_2 curing improved densification by $CaCO_3$ precipitation and partial rehydration, which resulted in a slight recovery but increased brittleness compared to water curing.
- Water-glass curing showed little improvement due to the silicate-rich surface layer hindering carbonation and hydration, whereas air curing resulted in drying shrinkage and microstructural coarsening, accelerating degradation.
- The property development of fire-damaged SCC is determined by the interplay of thermal decomposition, rehydration, and carbonation. Water re-curing was the most effective in restoring mechanical and microstructural performance among the regimens studied, followed by CO_2 curing.

Data availability

The datasets used and/or analyzed during the current study available from the corresponding author on reasonable request.

Received: 20 March 2025; Accepted: 10 September 2025
Published online: 14 October 2025

References

1. Aslani, F. & Samali, B. Constitutive relationships for self-compacting concrete at elevated temperatures. *Mater. Struct.* **48**, 337–356 (2015).
2. Zhang, H. Y. et al. Spalling behavior of metakaolin-fly Ash based geopolymer concrete under elevated temperature exposure. *Cem. Concr Compos.* **106**, 103483 (2020).
3. Novak, J. & Kohoutkova, A. Mechanical properties of concrete composites subject to elevated temperature. *Fire Saf. J.* **95**, 66–76 (2018).
4. Surya, T. R. et al. Compressive strength of self compacting concrete under elevated temperature. *Mater. Today: Proc.* **40**, S83–S87 (2021).
5. Fares, H., Noumowe, A. & Remond, S. Self-consolidating concrete subjected to high temperature: mechanical and physicochemical properties. *Cem. Concr Res.* **39**, 1230–1238 (2009).
6. Fares, H. et al. High temperature behaviour of self-consolidating concrete: microstructure and physicochemical properties. *Cem. Concr Res.* **40**, 488–496 (2010).
7. Pathak, N. & Siddique, R. Effects of elevated temperatures on properties of self-compacting-concrete containing fly Ash and spent foundry sand. *Constr. Build. Mater.* **34**, 512–521 (2012).
8. Janotka, I. & Mojumdar, S. Thermal analysis at the evaluation of concrete damage by high temperatures. *J. Therm. Anal. Calorim.* **81**, 197–203 (2005).
9. Xargay, H. et al. Temperature effects on failure behavior of self-compacting high strength plain and fiber reinforced concrete. *Constr. Build. Mater.* **165**, 723–734 (2018).
10. Pineaud, A. et al. Mechanical properties of high performance self-compacting concretes at room and high temperature. *Constr. Build. Mater.* **112**, 747–755 (2016).
11. Persson, B. Fire resistance of self-compacting concrete SCC. *Mater. Struct.* **37**, 575–584 (2004).
12. Reinhardt, H. W. & Stegmaier, M. Self-consolidating concrete in fire. *ACI Mater. J.* **103**, 130 (2006).
13. Xuan, D., Zhan, B. & Poon, C. S. Thermal and residual mechanical profile of recycled aggregate concrete prepared with carbonated concrete aggregates after exposure to elevated temperatures. *Fire Mater.* **42**, 134–142 (2018).
14. Bingöl, A. F. & Gül, R. Effect of elevated temperatures and cooling regimes on normal strength concrete. *Fire Mater.* **33**, 79–88 (2009).
15. Kalifa, P., Menneteau, F. D. & Quenard, D. Spalling and pore pressure in HPC at high temperatures. *Cem. Concr Res.* **30**, 1915–1927 (2000).
16. Kalifa, P., Chene, G. & Galle, C. High-temperature behaviour of HPC with polypropylene fibres: from spalling to microstructure. *Cem. Concr Res.* **31**, 1487–1499 (2001).
17. Andiç-Çakır, O. & Hızal, S. Influence of elevated temperatures on the mechanical properties and microstructure of self consolidating lightweight aggregate concrete. *Constr. Build. Mater.* **34**, 575–583 (2012).
18. Fu, Y. F. et al. Experimental study of micro/macro crack development and stress–strain relations of cement-based composite materials at elevated temperatures. *Cem. Concr Res.* **34**, 789–797 (2004).
19. Ma, Q. et al. Mechanical properties of concrete at high temperature—a review. *Constr. Build. Mater.* **93**, 371–383 (2015).
20. Rodrigues, F. & Joekes, I. Cement industry: sustainability, challenges and perspectives. *Environ. Chem. Lett.* **9**, 151–166 (2011).
21. Ouda, A. S. Development of high-performance heavy density concrete using different aggregates for gamma-ray shielding. *Prog Nucl. Energy*. **79**, 48–55 (2015).
22. Ouda, A. S. & Abdelgader, H. S. Assessing the physical, mechanical properties, and c-ray Attenuation of heavy density concrete for radiation shielding purposes. *Geosyst. Eng.* **22**, 72–80 (2019).
23. Aslani, F., Hamidi, F. & Ma, Q. Fire performance of heavyweight self-compacting concrete and heavyweight high strength concrete. *Materials* **12**, 822 (2019).
24. Gencel, O. Effect of elevated temperatures on mechanical properties of high strength concrete containing varying proportions of hematite. *Fire Mater.* **36**, 217–230 (2012).
25. Aslani, F. & Asif, Z. Properties of ambient-cured normal and heavyweight geopolymer concrete exposed to high temperatures. *Materials* **12**, 740 (2019).
26. Horszczaruk, E., Sikora, P. & Zaporowski, P. Mechanical properties of shielding concrete with magnetite aggregate subjected to high temperature. *Procedia Eng.* **108**, 39–46 (2015).
27. Horszczaruk, E. et al. The effect of elevated temperature on the properties of cement mortars containing Nanosilica and heavyweight aggregates. *Constr. Build. Mater.* **137**, 420–431 (2017).
28. Ling, T. C. & Poon, C. S. High temperatures properties of barite concrete with cathode ray tube funnel glass. *Fire Mater.* **38**, 279–289 (2014).
29. González-Ortega, M. A., Cavalaro, S. & Aguado, A. Influence of barite aggregate friability on mixing process and mechanical properties of concrete. *Constr. Build. Mater.* **74**, 169–175 (2015).
30. Bisby, L. A. et al. Strengthening fire-damaged concrete by confinement with fibre-reinforced polymer wraps. *Eng. Struct.* **33**, 3381–3391 (2011).
31. Yaqub, M. & Bailey, C. G. Repair of fire damaged circular reinforced concrete columns with FRP composites. *Constr. Build. Mater.* **25**, 359–370 (2011).
32. Crook, D. N. & Murray, M. J. Regain of strength after firing of concrete. *Mag Concr Res.* **22**, 149–154 (1970).
33. Lin, W. M. & Lin, T. D. Powers-Couche, L. J. Microstructures of fire-damaged concrete. *ACI Mater. J.* **93**, 199–205 (1996).
34. Poon, C. S., Azhar, S., Anson, M. & Wong, Y. L. Strength and durability recovery of fire-damaged concrete after post-fire-curing. *Cem. Concr Res.* **31**, 1307–1318 (2001).
35. Li, Q., Yuan, G. & Shu, Q. Effects of heating/cooling on recovery of strength and carbonation resistance of fire-damaged concrete. *Mag Concr Res.* **66**, 925–936 (2014).
36. Yaragal, S., Kittur, M. & Narayan, K. Recuring studies on concretes subjected to elevated temperatures and suddenly cooled by water quenching. *J. Struct. Fire Eng.* **6**, 67–76 (2015).
37. Chromá, M., Vo, D. & Bayer, P. Concrete rehydration after heating to temperatures of up to 1200°C. *Int. Conf. Durab. Build. Mater. Compon.* 1633–1639 (2011).
38. Alonso, C. & Fernandez, L. Dehydration and rehydration processes of cement paste exposed to high temperature environments. *J. Mater. Sci.* **39**, 3015–3024 (2004).
39. Shui, Z. et al. Cementitious characteristics of hydrated cement paste subjected to various dehydration temperatures. *Constr. Build. Mater.* **23**, 531–537 (2009).
40. Li, L. et al. A review on the recovery of fire-damaged concrete with post-fire-curing. *Constr. Build. Mater.* **237**, 117564 (2020).
41. Qian, Y., Yang, D., Xia, Y., Gao, H. & Ma, Z. Properties and improvement of ultra-high performance concrete with coarse aggregates and polypropylene fibers after high-temperature damage. *Constr. Build. Mater.* **364**, 129925 (2023).
42. Henry, M., Suzuki, M. & Kato, Y. Behavior of fire-damaged mortar under variable re-curing conditions. *ACI Mater. J.* **108**, 281–289 (2011).
43. Poon, C. S. et al. Strength and durability recovery of fire-damaged concrete after post-fire-curing. *Cem. Concr Res.* **31**, 1307–1318 (2001).
44. Lin, W. M., Lin, T. D. & Powers-Couche, L. J. Microstructures of Fire-Damaged concrete. *ACI Mater. J.* **93**, 199–205 (1996).

45. Onyelowe, K. C. et al. Mechanical properties of self-compacting concrete reinforced with hybrid fibers and industrial wastes under elevated heat treatment. *Sci. Rep.* **15**, 12753 (2025).
46. Bouhafs, F. et al. Effect of water re-curing on the physico-mechanical and microstructural properties of self-compacting concrete exposed to high temperatures. *Constr. Build. Mater.* **413**, 134805 (2024).
47. Lin, Y. et al. The effect of post-fire-curing on strength–velocity relationship for nondestructive assessment of fire-damaged concrete strength. *Fire Saf. J.* **46**, 178–185 (2011).
48. Li, L. et al. Effects of cement dosage and cooling regimes on the compressive strength of concrete after post-fire-curing from 800°C. *Constr. Build. Mater.* **142**, 208–220 (2017).
49. EFNARC. Best practices guidelines for self-consolidating concrete. (2002).
50. EFNARC. Specification and guidelines for self-compacting concrete. (2005).
51. European Standard No. 2390-3. Testing hardened concrete part 3: Compressive strength of test specimens. (2001).
52. ASTM C 642. Density absorption and voids in hardened concrete. (2006).
53. ASTM-C597. Standard test method for pulse velocity through concrete. (2002).
54. Galan, I., Andrade, C. & Castellote, M. Natural and accelerated CO2 binding kinetics in cement paste at different relative humidities. *Cem. Concr Res.* **49**, 21–28 (2013).
55. López-Arce, P. et al. Influence of relative humidity on the carbonation of calcium hydroxide nanoparticles and the formation of calcium carbonate polymorphs. *Powder Technol.* **205**, 263–269 (2011).
56. Ismaeel, N. S. & Khalaf, M. A. Properties of high strength concrete containing stonepowder as natural pozzolanic materials. *J. Univ. Anbar Pure Sci.* **7**, (2013).
57. Cheah, C. B. et al. The engineering properties and microstructure development of cement mortar containing high volume of inter-grinded GGBS and PFA cured at ambient temperature. *Constr. Build. Mater.* **122**, 683–693 (2016).
58. Bazant, Z. P. Size effect in blunt fracture: concrete, rock, metal. *J. Eng. Mech. ASCE.* **110**, 518–535 (1984).
59. Aslani, F. et al. High-performance fibre-reinforced heavyweight self-compacting concrete: analysis of fresh and mechanical properties. *Constr. Build. Mater.* **232**, 117230 (2020).
60. Park, S. J., Yim, H. J. & Kwak, H. G. Effects of post-fire curing conditions on the restoration of material properties of fire-damaged concrete. *Constr. Build. Mater.* **99**, 90–98 (2015).
61. Bensted, J. & Varma, S. P. Some applications of infrared and Raman spectroscopy in cement chemistry. *Cem. Technol.* **5**, 440–445 (1974).
62. He, F., Biolzi, L. & Carvelli, V. Effects of elevated temperature and water re-curing on fracture process of hybrid fiber reinforced concretes. *Eng. Fract. Mech.* **276**, 108885 (2022).
63. Song, W., Li, C. & Zhang, Y. Effects of post-fire rehydration on the mechanical and microstructural properties of slag-modified concrete. *Sci. Rep.* **13**, 136 (2023).
64. Rodriguez-Blanco, J. D., Shaw, S. & Benning, L. G. The kinetics and mechanisms of amorphous calcium carbonate (ACC) crystallization to calcite, via vaterite. *Nanoscale* **3**, 265–271 (2011).
65. Ylmén, R. & Jäglid, U. Carbonation of Portland cement studied by diffuse reflection fourier transform infrared spectroscopy. *Int. J. Concr Struct. Mater.* **7**, 119–125 (2013).
66. Yu, P. et al. Structure of calcium silicate hydrate (C-S- H): Near- , Mid- , and Far- infrared spectroscopy. *J. Am. Ceram. Soc.* **82**, 742–748 (1999).
67. Ni, M. & Ratner, B. D. Differentiating calcium carbonate polymorphs by surface analysis techniques—an XPS and TOF-SIMS study. *Surf. Interface Anal.* (2008).
68. Balmain, J., Hannoyer, B. & Lopez, E. Fourier transform infrared spectroscopy (FTIR) and x-ray diffraction analyses of mineral and organic matrix during heating of mother of Pearl (nacre) from the shell of the mollusc pinctada maxima. *J. Biomed. Mater. Res.* **48**, 749–754 (1999).
69. Higl, J. et al. Detailed in situ ATR-FTIR spectroscopy study of the early stages of C-S-H formation during hydration of monoclinic C3S. Cem. *Concr Res.* **142**, 106367 (2021).
70. Shen, Y. et al. Study on the Preparation and formation mechanism of barium sulphate nanoparticles modified by different organic acids. *J. Chem. Sci.* **119**, 319–324 (2007).
71. Saikia, B. J. Spectroscopic Estimation of geometrical structure Elucidation in natural SiO2 crystal. *J. Mater. Phys. Chem.* **2**, 28–33 (2014).
72. Russell, J. D. & Fraser, A. R. Infrared methods. In *Clay Mineralogy: Spectroscopic Chem. Determinative Methods* 11–67 (1994).
73. Yue, Y. et al. Raman spectroscopic investigation of friedel's salt. *Cem. Concr Compos.* **86**, 306–314 (2018).
74. Trezza, M. A. & Lavat, A. E. Analysis of the system 3CaO·Al2O3–CaSO4·2H2O–CaCO3–H2O by FT-IR spectroscopy. *Cem. Concr Res.* **31**, 869–872 (2001).
75. Timón, V. et al. Infrared and Raman vibrational modelling of β-C2S and C3S compounds. *Cem. Concr Res.* **169**, 107162 (2023).
76. Stepkowska, E. T. et al. Phase transformation on heating of an aged cement paste. *Thermochim Acta.* **420**, 79–87 (2004).
77. Tantawy, M. Effect of high temperatures on the microstructure of cement paste. *J. Mater. Sci. Chem. Eng.* **5**, 33–48 (2017).
78. Liu, T. et al. Strength recovery of thermally damaged high-performance concrete subjected to post-fire carbonation curing. *Cem. Concr Compos.* **143**, 105273 (2023).
79. Yousuf, M. et al. An FTIR and XPS investigations of the effects of carbonation on the solidification/stabilization of cement based systems-Portland type V with zinc. *Cem. Concr Res.* (1993).
80. Medvedev, E. F., Komarevskaya, A., Sh. IR spectroscopic study of the phase composition for sodium silicate synthesized in aqueous medium. *Glass Ceram.* **64**, 7–11 (2007).
81. Metha, P. K. & Monterio, P. J. M. Concrete, microstructure, properties and materials (2006).
82. Laskar, A. I., Kumar, R. & Bhattacharjee, B. Some aspects of evaluation of concrete through mercury intrusion porosimetry. *Cem. Concr Res.* **27**, 93–105 (1997).
83. Kumar, R. & Bhattacharjee, B. Study on some factors affecting the results in the use of MIP method in concrete research. *Cem. Concr Res.* **33**, 417–424 (2003).
84. Li, Y. et al. Effect of post-fire lime-saturated water and water–CO2 Cyclic curing on strength recovery of thermally damaged high-performance concrete with different silica contents. *Cem. Concr Res.* **164**, 107050 (2023).
85. Arandigoyen, M. et al. Variation of microstructure with carbonation in lime and blended pastes. *Appl. Surf. Sci.* **252**, 7562–7571 (2006).
86. Kutchko, B. G. et al. Degradation of well cement by CO2 under geologic sequestration conditions. *Environ. Sci. Technol.* **41**, 4787–4792 (2007).
87. Akca, A. H. & Özyurt, N. Deterioration and recovery of FRC after high temperature exposure. *Cem. Concr Compos.* **93**, 260–273 (2018).
88. Xi, X. et al. Influence of water glass modulus and alkali content on the properties of alkali-activated thermally activated recycled cement. *Constr. Build. Mater.* **452**, 138867 (2024).
89. Scrivener, K. L. Backscattered electron imaging of cementitious microstructures: Understanding and quantification. *Cem. Concr Compos.* **26**, 935–945 (2004).
90. Shah, V. et al. Changes in microstructure characteristics of cement paste on carbonation. *Cem. Concr Res.* **109**, 184–197 (2018).
91. Wang, H., Lyu, H., Liu, T., Li, Y. & Tan, K. H. Effect of post-fire curing on compressive strength of ultra-high performance concrete and mortar. *Constr. Build. Mater.* **346**, 128447 (2022).

Acknowledgements
This work was financially supported by the Slovak Research and Development Agency under the contracts APVV-23-0383 and APVV-19-0490, the Slovak Grant Agency VEGA under contracts N° 2/0080/24.

Author contributions
Taher A. Tawfik: Original draft; Writing—review & editing; Methodology; Formal analysis; Data curation; Investigation. Marti T. Palou: Project Methodology; Investigation. František Šoukal: Methodology; Formal analysis. Eva Kuzielová: Data curation; Formal analysis; Investigation; Writing—original draft, review & editing. Peter Peciar: Methodology; Formal analysis. Mahmoud Gharieb: Review & editing; Formal analysis. Sheelan Mahmoud Hama: Review & editing; Formal analysis. Jozef Švorec: Methodology; Formal analysis.

Declarations

Competing interests
The authors declare no competing interests.

Additional information
Correspondence and requests for materials should be addressed to T.A.T.

Reprints and permissions information is available at www.nature.com/reprints.

Publisher's note Springer Nature remains neutral with regard to jurisdictional claims in published maps and institutional affiliations.